Geochemistry, Geophysics, Geosystems®

Key Points:
- We study systematically the impact of different crustal and lithospheric mantle viscosities on stresses and velocities
- Simple analytical estimates for crustal deviatoric stress and horizontal velocity agree with 3D numerical results
- The double curvature of the Earth has a minor impact on the 3D stress distribution around the Tibetan plateau

Correspondence to:
E. Macherel,
emilie.macherel@unil.ch

3D Stresses and Velocities Caused by Continental Plateaus: Scaling Analysis and Numerical Calculations With Application to the Tibetan Plateau

Emilie Macherel[1] , **Ludovic Räss[1,2,3]**, and **Stefan M. Schmalholz[1]**

[1]ISTE, University of Lausanne, Lausanne, Switzerland, [2]Laboratory of Hydraulics, Hydrology and Glaciology (VAW), ETH Zurich, Zurich, Switzerland, [3]Swiss Federal Institute for Forest, Snow and Landscape Research (WSL), Birmensdorf, Switzerland

Abstract Understanding stresses is crucial for geodynamics since they govern rock deformation and metamorphic reactions. However, the magnitudes and distribution of crustal stresses are still uncertain. Here, we use a 3D numerical model in spherical coordinates to investigate stresses and velocities that result from lateral crustal thickness variations around continental plateaus like those observed for the Tibetan plateau. We do not consider any far-field deformation so that the plateau deforms by horizontal dilatation and vertical thinning. We assume viscous creep, a simplified plateau geometry, and simplified viscosity and density distributions to couple the numerical results with a scaling analysis. Specifically, we study the impact of the viscosity ratio between crust and lithospheric mantle, a rectangular plateau corner, a stress-dependent power-law flow law and Earth's double curvature on the crustal stress field and horizontal velocities. Two orders of magnitude variation in crustal and lithospheric mantle viscosities change the maximum crustal differential stress only by a factor of ≈ 2. We derive simple analytical estimates for the crustal deviatoric stress and horizontal velocity which agree to first order with 3D numerical calculations. We apply these estimates to calculate the average crustal viscosity in the eastern Tibetan plateau as $\approx 10^{22}$ Pa · s. Furthermore, our results show that a corner strongly affects the stress distribution, particularly the shear stresses, while Earth's curvature has a minor impact on the stresses. We further discuss potential implications of our results to strike-slip faulting and fast exhumation around the Tibetan plateau's syntaxes.

Plain Language Summary This study focuses on understanding the stresses in the Earth's crust, which is crucial for understanding how rocks deform and undergo chemical reactions. However, there is still uncertainty about the exact magnitudes and distribution of these stresses, especially in three dimensions (3D). To estimate long-term stresses in the lithosphere, scientists often use observed variations in the thickness of the Earth's crust around continental plateaus, like the Tibetan plateau which has an average altitude of approximately 5 km. The plateaus we study will flow apart under gravity on geological time scales to reduce the altitude difference between the plateau and neighboring lowlands, a process often termed gravitational collapse. Here, a 3D numerical model is used to explore the magnitudes and distribution of stress around these plateaus. The study considers factors like variations in the viscosity (a measure of a material's resistance to flow) of different parts of the lithosphere and the Earth's curvature. We derive simple mathematical equations to estimate the crustal stress and horizontal velocity and we test these estimates with the results of the performed 3D numerical calculations. The results further show that Earth's curvature has a minor impact on the stress distribution.

1. Introduction

Stress is a crucial quantity for geodynamic processes since it governs rock deformation (e.g., Karato, 2008; Turcotte & Schubert, 2014) and metamorphic reactions (e.g., Philpotts & Ague, 2022). Hence, many studies have focused on various aspects of stresses in the lithosphere, such as their sources, magnitude, distribution, or orientation (e.g., Artyushkov, 1973; Bott & Kusznir, 1984; Engelder, 2014; Frank, 1972; McGarr & Gay, 1978; Turcotte & Oxburgh, 1976; Zoback, 1992). It has been known for more than a hundred years that the existence of dry land and any differences in height on the Earth's surface is decisive evidence that the stress in the Earth is not hydrostatic, or lithostatic (e.g., Darwin, 1882; Jeffreys, 1932). Therefore, mountain ranges, continental plateaus, and continental tectonic plates cannot be in a lithostatic state of stress and must exhibit differential stresses, even if
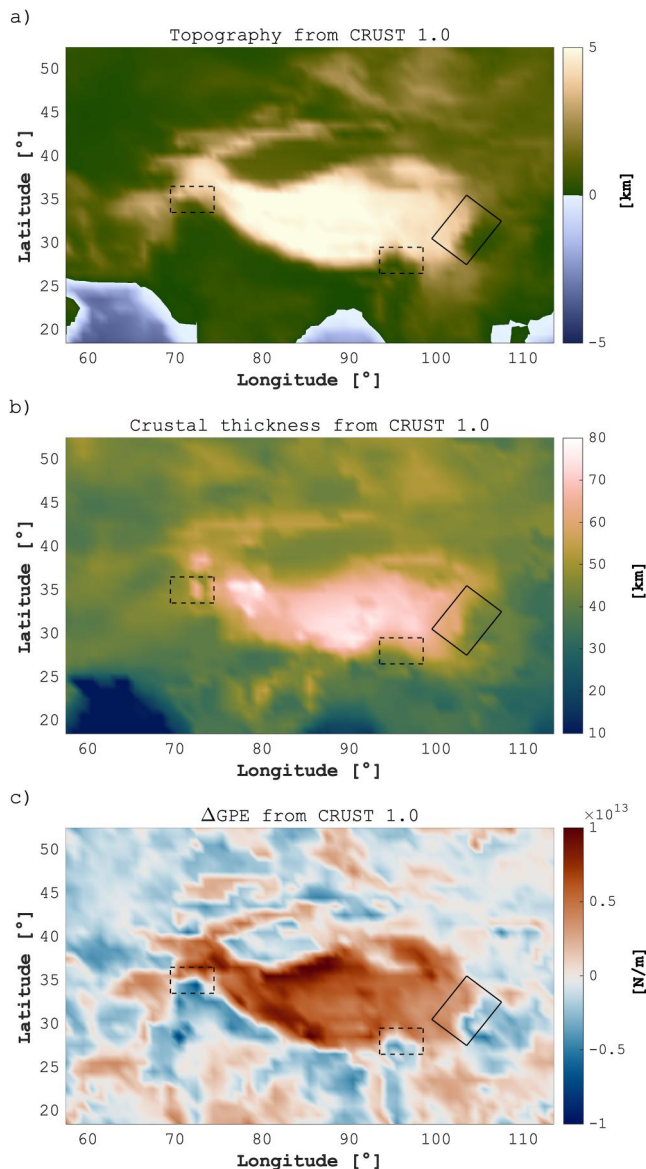
a)

b)

c)

Figure 1. Map view of the (a) topography, (b) crustal thickness, and (c) lateral variations of gravitational potential energy per unit area (ΔGPE) of the Tibetan plateau and its surroundings using the CRUST 1.0 data set (http://igppweb.ucsd.edu/~gabi/rem.html). The black rectangle indicates the region in which the Longmen Shan is located and the two dashed rectangles indicate the regions in which the two syntaxes are located (see Section 4.9).

they do not deform significantly (e.g., Frank, 1972; Jeffreys, 1932). However, the magnitudes of these differential stresses in the lithosphere, especially in the continental crust, remain still debated (e.g., Hardebeck & Okada, 2018; Kanamori, 1980). For example, the median value of stress drop from earthquakes is approximately 4 MPa for all fault types and this value is approximately constant with depth (e.g., Allmann & Shearer, 2009). Some studies propose that such stress drops measure a quantity that is close to the total crustal stress because of, for example, the rotation of the principal stress axes following earthquakes (e.g., Hardebeck & Okada, 2018). Such studies imply that the continental crust is mechanically weak (e.g., Hardebeck & Okada, 2018). In contrast, stress estimates from, for example, boreholes provide differential stresses of ≈150 MPa at a depth of 8 km (Townend & Zoback, 2000). Such studies imply that the continental crust, at least the upper crust, is mechanically strong.

Here, we apply a scaling analysis in combination with 3D numerical calculations to estimate crustal stresses around continental plateaus. In the absence of any far-field deformation, a continental plateau will deform by horizontal dilatation and vertical thinning, a process that is frequently termed gravitational collapse (e.g., Rey et al., 2001). A common method to estimate the vertically averaged lithospheric stress around continental plateaus, or mountains in general, is based on vertical integrals of the two-dimensional (2D) force balance equations (e.g., Dalmayrac & Molnar, 1981; Fleitout & Froidevaux, 1982; Molnar & Lyon-Caen, 1988). With this method, the vertical integral of the horizontal differential stress across the lithosphere can be estimated from the lateral variations of crustal thickness and topography (e.g., Artyushkov, 1973; Frank, 1972; Jeffreys, 1932) or, more generally, from lateral variations of the gravitational potential energy per unit area, GPE (e.g., Molnar & Lyon-Caen, 1988; Molnar et al., 1993; Parsons & Richter, 1980; Schmalholz et al., 2014, 2019). These integrated stress estimates result from the force balance in the lithosphere and are, hence, robust because they are independent of constitutive equations, such as creep flow laws, and require only representative values for topography, crustal thickness, and densities of the crust and lithospheric mantle, which are well constrained (Figure 1). We consider here typical values for topography, crustal thickness, and densities for the Tibetan plateau. The Tibetan plateau is the largest continental plateau on Earth, exhibiting an average topography of ≈5 km and a crustal thickness of ≈70 km (e.g., Kind et al., 2002; Nábělek et al., 2009; Royden et al., 2008) (Figure 1). For the Tibetan plateau, GPE-based estimates for the vertically integrated stress vary between $0.7 \cdot 10^{13}$ and 10^{13} N/m (Figure 1c), and the corresponding vertically averaged stresses are between 70 and 100 MPa for a 100 km thick lithosphere (e.g., Molnar & Lyon-Caen, 1988; Molnar et al., 1993; Schmalholz et al., 2014, 2019).

The disadvantage of the GPE-based stress estimates is that they cannot resolve the relative magnitudes of stresses in the crust and lithospheric mantle. Therefore, the relative contributions of the continental crust and the lithospheric mantle to the long-term stress and strength of the lithosphere remain unclear. For example, some studies on the Tien Shan propose that the major part (up to 90%) of the lithospheric strength resides in the ductile lithospheric mantle (e.g., England & Molnar, 2015). In contrast, other studies argue that a significant part of the lithospheric strength, required to support the Tibetan plateau, resides in the seismogenic upper crust (e.g., Flesch et al., 2001). A strong crust is also supported by full 2D numerical lithospheric models, considering vertical viscosity and stress variations (Schmalholz et al., 2019). These 2D models show that the topographic variation between the Tibetan plateau and lowland essentially disappears due to horizontal dilatation and vertical thinning within less than 1 Myr if shear stresses in the crust are limited to 5 MPa (like the median value of stress drops), even for a lithospheric mantle with significant strength (Schmalholz
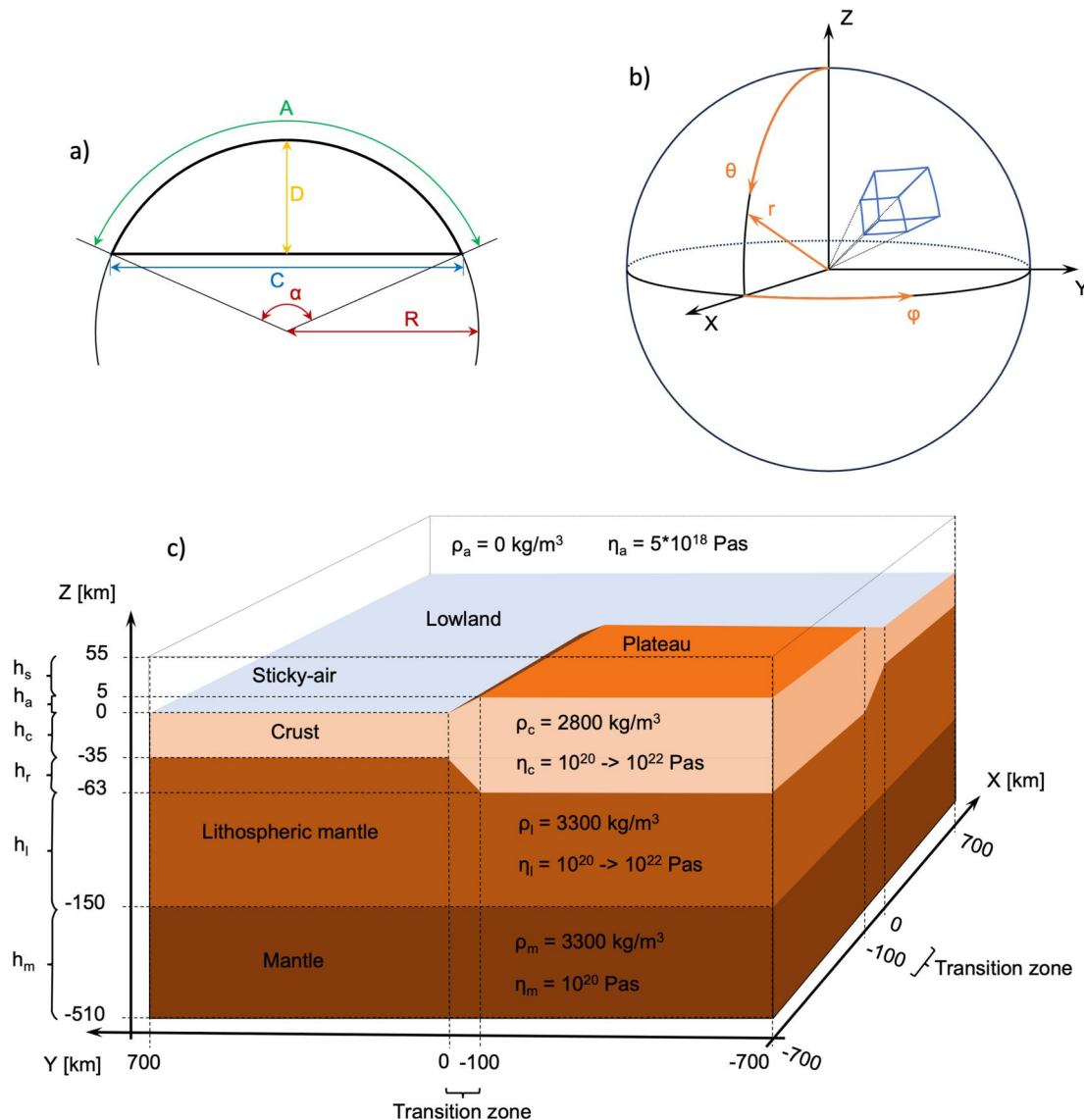
Figure 2. (a) Sketch of a circular segment indicating the geometric quantities used for the shallow sheet scaling. R, Earth's radius; A, arc length; C, chord length; D, height of segment; α, central angle. (b) Spherical coordinate system. The model domain (blue box) is defined at the surface of a sphere of various radii (e.g., the Earth's radius). (c) Model configuration, for simplicity sketched in Cartesian coordinates: a cube of size 565 km vertically and 1,400 km · 1,400 km horizontally, composed by four different layers representing the mantle, the lithospheric mantle, the continental crust, and sticky-air, from bottom to top. A continental plateau in isostatic equilibrium is defined on a quarter of the domain. Gravity acts in the vertical, r-direction.

et al., 2019). These 2D numerical models suggest that stress magnitudes in the crust must be considerably larger than 5 MPa, at least in some crustal levels such as the seismogenic upper crust, and that a strong lithospheric mantle alone is not sufficient to support the Tibetan plateau (Schmalholz et al., 2019).

To estimate crustal stresses and horizontal velocities around a continental plateau, we apply a 3D numerical model in which the viscosity of the crust and lithospheric mantle can be different. We consider both linear and power-law viscous flow. We apply a 3D model because we also want to quantify the impact of the plateau's corner on the stress field. The impact of corners was studied also with so-called thin viscous sheet models that are based on vertical integrals of the 3D force balance equations (e.g., Bird & Piper, 1980; England & Houseman, 1988; England & McKenzie, 1982; Houseman & England, 1986; Medvedev & Podladchikov, 1999). However, such thin viscous sheet models do not consider the rheological layering of the lithosphere, such as different viscosities of the crust and lithospheric mantle, as we consider here. We consider here a rectangular corner geometry to quantify the first-order impact of lateral geometrical variations on the stress field, particularly on the horizontal

Table 1
Mathematical Symbols Used in the Text

Symbol	Name or definition	Unit
L_r, L_θ, L_φ	Height, width, length of the model domain	[m]
r, θ, φ	Spherical coordinates	[m], [rad], [rad]
R	Radius	[m]
H	Thickness of the lithosphere	[m]
A, C, D	Arc length, chord length, height of circular segment	[m]
h_s, h_{st}	Sticky-air thickness	[m]
h_a	Altitude of the plateau	[m]
h_c	Crustal thickness in the lowland	[m]
h_r	Root thickness	[m]
h_l	Lithospheric mantle thickness	[m]
h_m	Mantle thickness	[m]
L	Length scale	[m]
λ	Width of a two-sided wedge	[m]
ρ_a	Sticky-air density	[kg/m^3]
ρ_c, ρ_l, ρ_m	Crustal, lithospheric mantle, mantle densities	[kg/m^3]
η_a, η_{st}	Sticky-air viscosity	[Pa · s]
η_c, η_l, η_m	Crustal, lithospheric mantle, mantle viscosities	[Pa · s]
η	Linear viscosity	[Pa · s]
η_E, η_{cE}	Effective viscosity	[Pa · s]
η_{ch}	Characteristic viscosity	[Pa · s]
α	Central angle	[°]
g	Gravitational acceleration	[m/s^2]
ΔGPE	Variations in gravitational potential energy	[N/m]
τ_C	Characteristic stress	[Pa]
τ, τ_e	Deviatoric stress, estimated deviatoric stress	[Pa]
τ_{II}	Second invariant of the deviatoric stress tensor	[Pa]
$(\sigma_1 - \sigma_3)$	Differential stress	[Pa]
$\dot{\epsilon}$	Strain rate	[1/year]
$\dot{\epsilon}_{II}$	Second invariant of the strain rate tensor	[1/year]
V_s, V_e	Horizontal velocity, estimated horizontal velocity	[cm/year]
V_{ePL}	Estimated horizontal velocity for power-law viscous crust	[cm/year]
V_{bs}	Basal shear velocity	[cm/year]
n	Power-law stress exponent	[−]

and vertical shear stresses. To evaluate the impact of both vertical viscosity variations and lateral geometry variations on the lithospheric stress field, full 3D numerical models are required (e.g., Bischoff & Flesch, 2019; L. Chen et al., 2020; Lechmann et al., 2014; Pusok & Kaus, 2015; Yang et al., 2020; P. Zhang et al., 2022). However, essentially all 3D numerical models focusing on the Tibetan plateau employ a rectangular model geometry and do not consider the potential impact of Earth's double curvature (e.g., L. Chen et al., 2020; Lechmann et al., 2014; Yang et al., 2020; P. Zhang et al., 2022). The double curvature of the Earth's lithosphere could potentially have an impact on its mechanical strength and stress state because mechanical studies demonstrate that small amounts of bending of plates reinforce the mechanical stability of thin sheets (e.g., Pini et al., 2016). Therefore, we evaluate here also the impact of curvature on the stress field around continental plateaus by comparing the results of a rectangular model with the results of spherical models having different radii of curvature.

Table 2
Values Used in This Study

Variable	Value
$L_r \cdot L_\theta \cdot L_\varphi$	565 km · 1,400 km · 1,400 km
R	$6{,}371 \cdot 10^3$ km, 6,371 km, 3,390 km, 1,737 km
h_s	50 km
h_a	5 km
h_c	35 km
h_r	28 km
h_l	87 km
h_m	360 km
ρ_a	0 kg/m^3
ρ_c	2,800 kg/m^3
ρ_l	3,300 kg/m^3
ρ_m	3,300 kg/m^3
η_a	$5 \cdot 10^{18}$ Pa · s
η_c	10^{20}–10^{22} Pa · s
η_l	10^{20}, 10^{21}, 10^{22} Pa · s
η_m	10^{20} Pa · s
g	9.81 m/s^2
τ_C	24 MPa
n	1, 3, 6

In our study, we aim (a) to quantify the magnitudes of differential stresses and horizontal velocities in the crust around continental plateaus, (b) to study the impact of viscosity differences between the crust and lithospheric mantle on the stress field and horizontal velocities, (c) to evaluate the impact of a rectangular corner on normal and shear stresses in the crust, (d) to investigate the impact of a stress-dependent, power-law viscous flow law on the crustal stress field and horizontal velocities, (e) to quantify the impact of double curvature on the stress field around continental plateaus and (f) to estimate deviatoric stresses, horizontal velocities and viscosities of the crust with simple analytical expressions.

2. Model

2.1. Geometrical Shallow Sheet Scaling for the Impact of Curvature

We start with a simple scaling analysis for the impact of curvature on our model for a continental plateau. We will consider in our model a lithosphere with lateral dimensions, L, of 1,400 km (Figure 2; the model configuration will be discussed in detail in Section 2.4). Considering the Earth's curvature, this lateral dimension corresponds to an arc length, A, on the curved Earth's surface (Figure 2a). All symbols used in the text are explained in Table 1 and the values applied in the calculations are given in Table 2. Our modeled lithosphere has a thickness, H, of 150 km. The lithosphere can be considered as a thin-shell because its thickness is much smaller than both its lateral dimension, and the radius of curvature of the Earth, $R = 6{,}371$ km (e.g., Ribe, 2002, 2018). Following Ribe (2018), we refer to a viscous shell as a sheet. Our model lithosphere can be considered as a shallow sheet if its "midsurface departs from a reference plane by an amount much smaller than its principal radii of curvature" (Ribe, 2018). To estimate the midsurface departure, we consider the chord, with length C, as the reference plane and the arc, with length A, as the curved midsurface (Figure 2a). The height of the circular segment represents the maximum departure, D, of the arc from the chord (Figure 2a). The height of the circular segment $D = R(1 - \cos(\alpha/2))$, where α is the central angle that is given by $\alpha = A/R$ (e.g., Bronstein et al., 2015) (Figure 2a). For $A = 1{,}400$ km and $R = 6{,}371$ km, $\alpha = \approx 12.6°$ and $D = \approx 38.4$ km. The ratio $D/R = 0.006$ and is, hence, significantly smaller than one. Therefore, the lithosphere in our model can be considered as a shallow sheet. Consequently, the differences in stress and velocity between a flat lithosphere and a curved lithosphere are likely in the order of the value of $H/L \approx 0.1$ (e.g., Ribe, 2018). Hence, we do not expect significant differences between the results of a flat and curved lithosphere. We will quantify these differences with 3D numerical calculations for a flat and several curved model geometries. A more detailed scaling analysis concerning thin shells is beyond the scope of this study and can be found in Ribe (2018).

2.2. Analytical Estimates for Stress and Velocity

Stress magnitudes in the lithosphere around continental plateaus can be estimated from lateral variations, or differences, of the gravitational potential energy per unit area, GPE (e.g., Dalmayrac & Molnar, 1981; Jeffreys, 1932; Molnar & Lyon-Caen, 1988). The GPE is the vertical integral of the lithostatic pressure (e.g., Molnar & Lyon-Caen, 1988). The difference in GPE, ΔGPE, between plateau and surrounding lowland is given by (e.g., Molnar & Lyon-Caen, 1988; Schmalholz et al., 2014)

$$\Delta \text{GPE} = \rho_c g h_a \left(h_c + \frac{\rho_l}{\rho_l - \rho_c} \frac{h_a}{2} \right) \tag{1}$$

where ρ_c, ρ_l, h_c, h_a and g are the crustal density, the lithospheric mantle density, the crustal thickness of the lowland, the altitude of the plateau and the gravitational acceleration, respectively (Figure 2c). The above expression for ΔGPE is derived assuming Airy isostasy (e.g., Molnar & Lyon-Caen, 1988; Schmalholz et al., 2014). The magnitude of ΔGPE corresponds to the horizontal driving force per unit length that is required to

mechanically support a continental plateau (e.g., Molnar & Lyon-Caen, 1988). Schmalholz et al. (2014) provide an estimate for the magnitude of the horizontal deviatoric stress, τ_e, that is vertically averaged across the crust:

$$\tau_e \approx \frac{\Delta \text{GPE}}{2(2h_c + h_a + h_r)} \tag{2}$$

where h_r is the thickness of the crustal root under the plateau (Figure 2c). Using the isostatic relation

$$h_r = \frac{\rho_c h_a}{\rho_l - \rho_c} \tag{3}$$

and the expression for ΔGPE from Equation 1 yields an expression for τ_e in the form of

$$\tau_e \approx \frac{\rho_c g h_a}{4}. \tag{4}$$

This stress estimate is independent of rheological parameters such as viscosity.

The ΔGPE between plateau and lowland will cause horizontal dilatation and vertical thinning of the continental plateau, a process often referred to as gravitational collapse (e.g., Rey et al., 2001). We assume that the crust behaves like a linear viscous fluid. The deviatoric stress, τ_e, in the crust generates a strain rate, $\dot{\epsilon}$, which depends on the crustal viscosity, η_c, and is given by the linear viscous flow law:

$$\dot{\epsilon} = \frac{\tau_e}{2\eta_c}. \tag{5}$$

We assume that $\dot{\epsilon}$ can be approximated by the ratio of the horizontal velocity, V_e, to a characteristic length, L, over which the horizontal extension of the plateau occurs:

$$\dot{\epsilon} \approx \frac{V_e}{L}. \tag{6}$$

Using Equations 4–6, we obtain an estimate for V_e:

$$V_e \approx \frac{\rho_c g h_a L}{8\eta_c}. \tag{7}$$

We will use the results of 3D numerical calculations to test the applicability of the estimate for the stress, Equation 4, to determine the characteristic length, L, and to test the estimate for the velocity V_e, Equation 7.

To assess the impact of more complicated viscous flow laws, we consider also a stress-dependent viscosity (e.g., Karato, 2008). We apply a combination of a linear and power-law viscous flow law for which the effective crustal viscosity, η_{cE}, is

$$\eta_{cE} = \frac{2\eta_c}{1 + \left(\frac{\tau_e}{\tau_C}\right)^{(n-1)}} \tag{8}$$

where n is the power-law stress exponent. For the analytical estimate, we assume that the effective viscosity is controlled by the deviatoric stress estimate, τ_e. τ_C defines the stress magnitude at which the deformation behavior changes from a linear viscous flow law to a power-law viscous flow law (e.g., Macherel, Podladchikov, et al., 2023; Schmalholz & Podladchikov, 2013). If $n = 1$, then $\eta_{cE} = \eta_c$, and the flow is linear viscous. For $n > 1$, $\eta_{cE} < \eta_c$ if $\tau_e > \tau_C$, an effect often referred to as stress weakening. If τ_e would become infinitely large, then η_{cE} would approach zero. Hence, the minimal possible value of $\eta_{cE} = 0$. Conversely, for $n > 1$, $\eta_{cE} > \eta_c$ if $\tau_e < \tau_C$, representing a hardening effect. If τ_e goes to zero then η_{cE} goes to $2\eta_c$. Hence, the maximal possible value of $\eta_{cE} = 2\eta_c$. The applied stress-dependent flow law, Equation 8, is useful to assess the impact of both weakening and

hardening compared to a linear viscosity, η_c, for $n = 1$. The flow law of Equation 8 is also frequently applied without the factor of 2 in the numerator to mimic a combined flow law with diffusion and dislocation creep. The difference compared to η_{cE} in Equation 8 is that for $n = 1$ the effective viscosity does not correspond to the linear viscosity.

To derive an equation for V_e for a power-law viscous crust, we use Equation 4 to replace τ_e in Equation 8 and then use this new expression for η_{cE} to replace η_c in Equation 7. The velocity estimate for a power-law viscous crust, V_{ePL}, is then:

$$V_{ePL} \approx \frac{\rho_c g h_a L}{16\eta_c}\left(1 + \left(\frac{\rho_c g h_a}{4\tau_C}\right)^{(n-1)}\right). \tag{9}$$

We normalize V_{ePL} by the velocity estimate for linear viscous flow for $n = 1$, V_e, to obtain a dimensionless velocity of the form

$$\frac{V_{ePL}}{V_e} \approx \frac{1}{2}\left(1 + \left(\frac{\rho_c g h_a}{4\tau_C}\right)^{(n-1)}\right). \tag{10}$$

We will compare the analytical estimates for the velocity for stress-dependent viscosities with the results of 3D numerical calculations.

2.3. Mathematical Model

We apply the so-called Stokes equations for slow, incompressible viscous flow under gravity in 3D (e.g., Malvern, 1969; Turcotte & Schubert, 2014). We consider a spherical coordinate system (Figure 2b). The corresponding equations of mass conservation and linear momentum conservation are displayed in Appendix A1. As for the analytical estimate, we employ a combination of a linear and power-law viscous flow law for which the effective viscosity, η_E, is (e.g., Gerya, 2019; Schmalholz & Podladchikov, 2013):

$$\eta_E = \frac{2\eta}{1 + \left(\frac{\tau_{II}}{\tau_C}\right)^{(n-1)}} \tag{11}$$

where η is the linear viscosity for $n = 1$, n is again the stress exponent and τ_C is again the characteristic stress controlling the transition from linear to power-law viscous flow. For the simulated 3D viscous flow, the stress magnitude that controls the effective viscosity is quantified by τ_{II} which is the second invariant of the deviatoric stress tensor and given by

$$\tau_{II} = \sqrt{0.5\,\tau_{ij}^2} \tag{12}$$

where symbols τ_{ij} represent the components of the deviatoric stress tensor, indices i and j represent the spherical coordinates r, θ, and φ, and the Einstein summation convention applies (Appendix A1 and Figure 2b). We apply the effective viscosity, η_E, in a flow law for the 3D viscous flow calculations:

$$\tau_{ij} = 2\eta_E \dot{\epsilon}_{ij} \tag{13}$$

where $\dot{\epsilon}_{ij}$ are the components of the deviatoric strain rate tensor. The applied flow law for the individual stress tensor and strain rate tensor components are given in Appendix A1. The applied numerical algorithm is written for spherical coordinates and the numerical method to solve the governing system of equations is described in Appendix A2.

2.4. Model Configuration

In the applied spherical coordinate system, r is the radial direction, θ is the polar angle ($\theta \in [0; \pi/2]$) and φ is the azimuthal angle ($\varphi \in [0; 2\pi]$; see Figure 2b). The geometry of the model domain represents a small 3D region from a sphere and its shape is like a rectangular cuboid that is deformed to adapt to the spherical geometry (Figure 2b). The model domain has a size of 565 km vertically and 1,400 km · 1,400 km horizontally measured at the surface of the sphere (Figure 2b). A continental plateau is configured on a quarter of the model domain with a horizontal size of 600 km · 600 km and a transition zone between the plateau and the surrounding lowland with a width of 100 km (Figure 2b). The model domain represents a quarter of a larger, quadratic (in map view) plateau that is entirely surrounded by lowland. The lateral model sides at Y = −700 km and X = −700 km, bounding the plateau in our model domain (see Figure 2b), represent symmetry planes for the deformation of the larger plateau that is entirely surrounded by lowland.

Vertically, the model domain is divided into four different layers, or model units, representing, from bottom to top, the asthenospheric mantle (referred to simply as mantle in the following), the lithospheric mantle, the continental crust, and a zero-density, weak layer that represents air, sometimes referred to as sticky-air layer (e.g., Crameri et al., 2012). The bottom layer has a constant thickness of 360 km, a density of 3,300 kg/m^3 and a linear viscosity of 10^{20} Pa · s. The lithospheric mantle has a thickness of 115 km below the lowland and 87 km below the plateau. It has a density of 3,300 kg/m^3 and we apply linear viscosities of 10^{20}, 10^{21}, and 10^{22} Pa · s in different simulations. The continental crust in the lowland is 35 km thick, to which are added 5 km of elevation and 28 km of root to form a plateau in isostatic equilibrium (e.g., Schmalholz et al., 2014). It has a density of 2,800 kg/m^3 and we vary its viscosity between 10^{20} and 10^{22} Pa · s in different simulations.

The sticky-air layer is applied to allow the surface of the crust to behave essentially as a free surface. It has a thickness of 55 km over the lowland and of 50 km over the plateau. Its density is 0 kg/m^3 and its linear viscosity is $5 \cdot 10^{18}$ Pa · s. The thickness and the viscosity of the sticky-air layer have been chosen following a criterion defined by Crameri et al. (2012). This criterion guarantees that the sticky-air layer is sufficiently weak and thick to mimic a free surface boundary condition. The ratio $\left(\eta_{st}/\eta_{ch}\right)/(h_{st}/L)^3$ has to be significantly smaller than one, where η_{st} and η_{ch} are the viscosity of the sticky-air and a characteristic viscosity value, respectively, h_{st} is the sticky-air thickness and L is a characteristic length of the model. For the values used in this study, $\eta_{st} = 5 \cdot 10^{18}$ Pa · s and $h_{st} = 50$ km. We consider $\eta_{ch} = 10^{20}$–10^{22} Pa · s and the order of magnitude of L is 100 km. Then, the ratio $\left(\eta_{st}/\eta_{ch}\right)/(h_{st}/L)^3$ ranges between 0.004 and 0.4. The applied sticky-air layer is, hence, suitable to mimic a free surface boundary condition. The boundary conditions applied in this study are free slip on each lateral side and at the top and bottom of the model domain. We do not prescribe any boundary velocity so that gravity, pointing toward the center of the coordinate system along direction r, is the only driving force acting in the model domain. The applied numerical resolution is 804 m vertically and 7.07 km horizontally, resulting from a numerical mesh with 703 · 199 · 199 grid points.

The applied model geometry and densities generate a ΔGPE between the plateau and the lowlands of $\approx 7 \cdot 10^{12}$ N/m. A ΔGPE of $\approx 7 \cdot 10^{12}$ N/m has been typically used in theoretical GPE studies applied to the Tibetan plateau (e.g., Molnar & Lyon-Caen, 1988; Schmalholz et al., 2014) and is a representative value of ΔGPE between the Tibetan plateau and its surrounding lowlands resulting from the CRUST1.0 data set (Laske et al., 2013) (Figure 1c).

Parameters related to the power-law flow law are the power-law exponent, n, and the characteristic stress, τ_C. In this study, we test three different values for the power-law exponent, $n = 1$ (linear viscous), $n = 3$ and $n = 6$. The values of $n > 1$ are only tested for a crustal linear viscosity $\eta_c = 10^{22}$ Pa · s in the equation for the effective viscosity, η_E (Equation 11). We investigate the impact of one value only for the characteristic stress τ_C and use $\tau_C = 24$ MPa. We choose this value because it represents average values of crustal stress. Hence, some crustal regions will exhibit stresses $> \tau_C$, and undergo stress weakening, and other regions will exhibit stresses $< \tau_C$, and undergo hardening.

The calculations are done with values in dimensionless form. Three characteristic scales are used to scale the results back to real physical units: one characteristic scale for length, which is the total height of the model domain; one scale for viscosity, which is the linear mantle viscosity; and one scale for density, which is the mantle density.
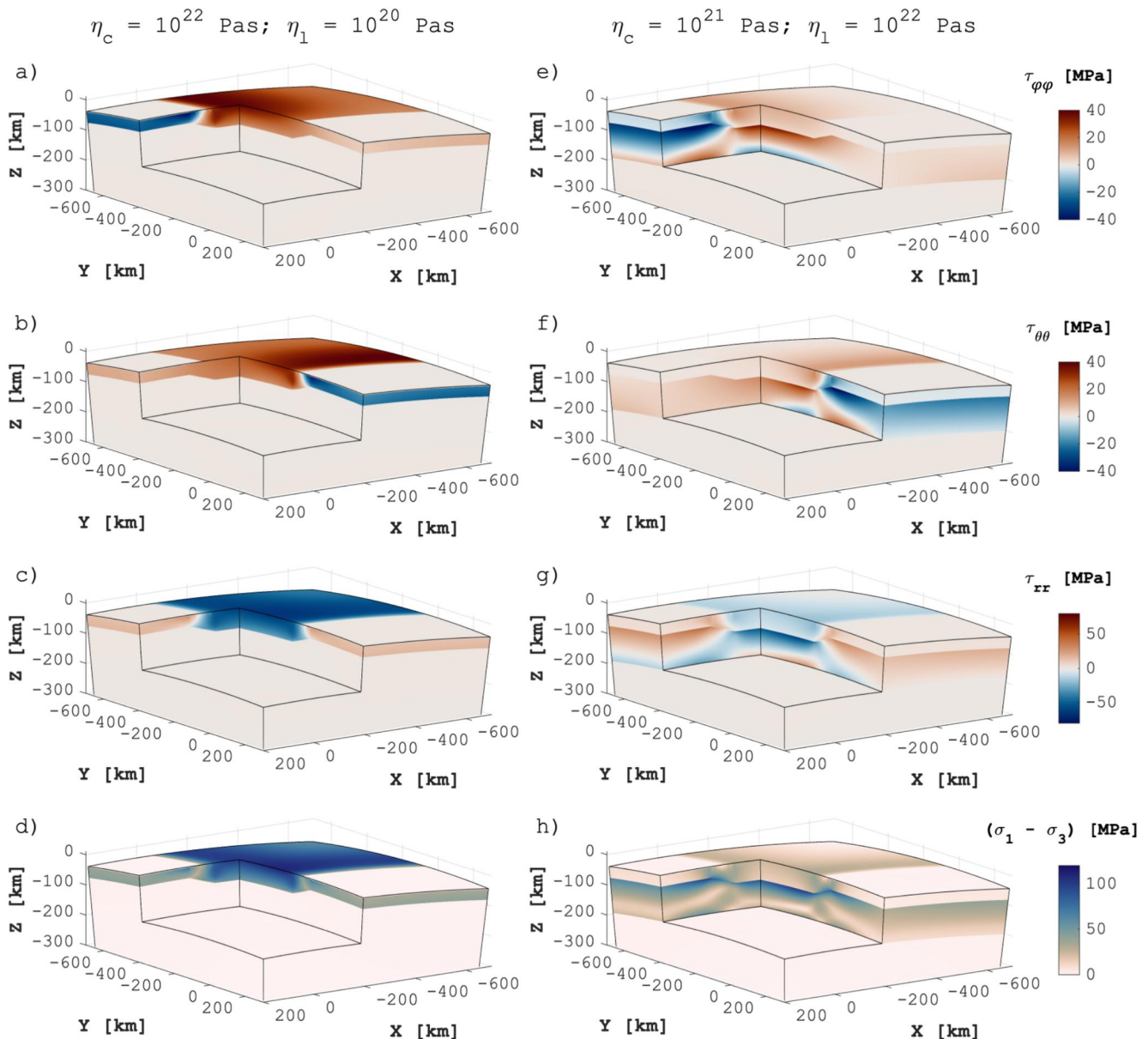
Figure 3. 3D visualization of deviatoric normal stresses in the direction parallel to the X-direction (panels a, e), parallel to Y (b, f), and parallel to Z (c, g). Panels (d) and (h) display the differential stress $(\sigma_1 - \sigma_3)$. Panels (a)–(d) show results for a simulation with a strong crust (10^{22} Pa · s) and a weak lithospheric mantle (10^{20} Pa · s), model SC_WL, and panels (e)–(h) for a simulation with an intermediate crust (10^{21} Pa · s) and a strong lithospheric mantle (10^{22} Pa · s), model IC_SL. Positive and negative deviatoric stress values indicate extensional and compressive stresses, respectively. These simulations are performed with the Earth's curvature and for linear viscous flow.

3. Results

3.1. Overview

We begin by presenting the 3D stress field for two representative simulations with linear viscous flow: A simulation with a mechanically strong crust (10^{22} Pa · s) and a weak lithospheric mantle (10^{20} Pa · s), referred to as model SC_WL in the following, and another simulation with a strong lithospheric mantle (10^{22} Pa · s) and crust with intermediate strength (10^{21} Pa · s), referred to as IC_SL. Next, we show the results of systematic simulations that evaluate the impact of the viscosity ratio between the crust and lithospheric mantle on the stress field and horizontal velocity. Afterward, we present results that show the impact of a rectangular corner on the stress field and simulations that show the impact of a power-law viscous flow law. Subsequently, we compare simulations
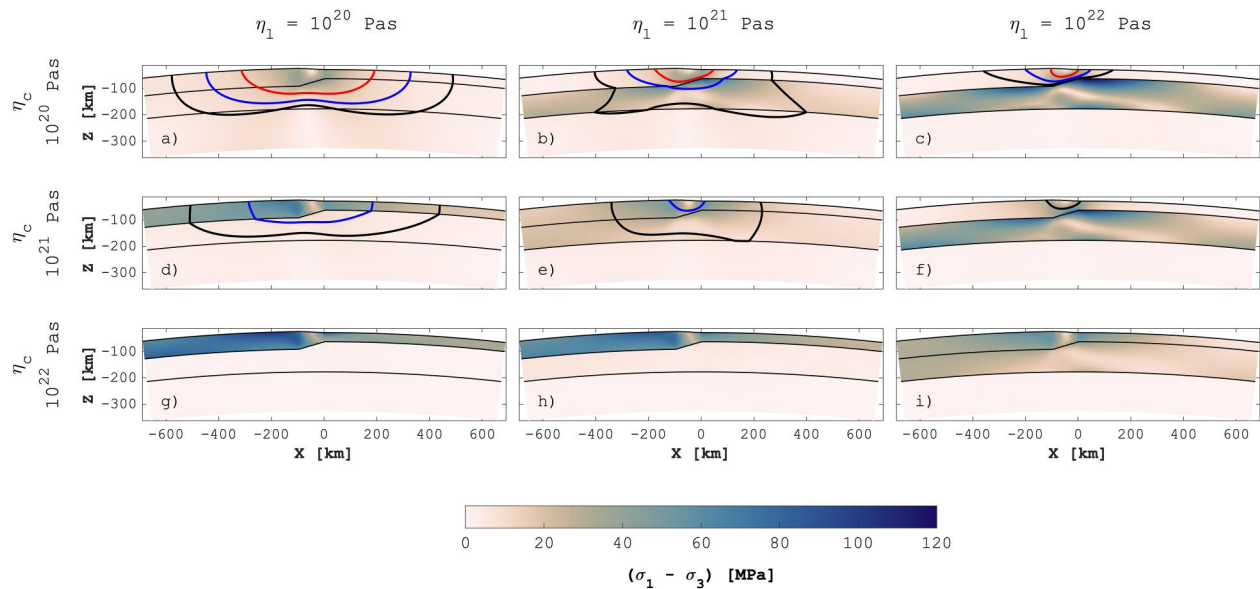
Figure 4. Vertical cross-sections at profile location HP1 for different models showing differential stress. Differential stress for crustal viscosities of 10^{20} Pa · s (a–c), 10^{21} Pa · s (d–f) and 10^{22} Pa · s (g–i) and lithospheric mantle viscosities of 10^{20} Pa · s (a, d, g), 10^{21} Pa · s (b, e, h) and 10^{22} Pa · s (c, f, i). The thick contour lines indicate horizontal velocities of black: 4 cm/year, blue: 10 cm/year, and red: 20 cm/year. The thin black lines display the limits between the continental crust, the lithospheric mantle, and the mantle. These simulations are done using the Earth's curvature and linear viscous flow.

with and without curvature to quantify the impact of lithospheric curvature on the stress field. Finally, we apply the numerical results to our scaling analysis and compare the analytical estimates for stress and velocity presented in Section 2.2 with the numerical results.

All numerical calculations are done for a curved model geometry corresponding to the curvature of the Earth, except the simulations that are performed to test the impact of curvature. For each model configuration, we have calculated a single time step to obtain the instantaneous 3D stress and velocity fields. For visualization reasons, we display the results for the spherical coordinates in a Cartesian coordinate system.

3.2. General Stress State Around a Continental Plateau

Figure 3 shows for two simulations (Figures 3a–3d: SC_WL and Figures 3e–3h: IC_SL) the three deviatoric normal stresses in the three spatial directions and the differential stress $(\sigma_1 - \sigma_3)$, that is the difference between the largest and the smallest principal stress at each numerical grid point of the model domain.

For the model SC_WL, high stress magnitudes are inside the crust and are essentially zero in the mantle and lithospheric mantle (Figures 3a–3d). Conversely, for the model IC_SL, stress magnitudes are larger in the lithospheric mantle compared to the crust (Figures 3e–3h). In general, in both horizontal directions, the same stress pattern is visible: an extension of the plateau (positive deviatoric stresses) and a compression of the surrounding lowland (negative deviatoric stresses). This stress pattern represents the horizontal dilatation of the continental plateau. The negative vertical deviatoric stress values located inside the plateau indicate a vertical thinning of the crust (Figures 3c and 3g). Furthermore, the magnitudes of the vertical deviatoric stresses are twice larger than the ones of the horizontal deviatoric stresses. The relation between the deviatoric normal stresses is constrained because the sum of the deviatoric normal stresses is zero by definition (e.g., Malvern, 1969).

Figure 3d shows that for model SC_WL the largest differential stresses are located inside the plateau. The largest differential stresses for model IC_SL are located below the plateau at the top of the lithospheric mantle (Figure 3h). Differential stresses are also high below the lowlands at the top of the lithospheric mantle (Figure 3h).

In summary, the ratio of crustal viscosity to the lithospheric mantle viscosity has a major impact on the distribution and magnitude of stresses in the crust and lithospheric mantle. If the lithospheric mantle is weak, then
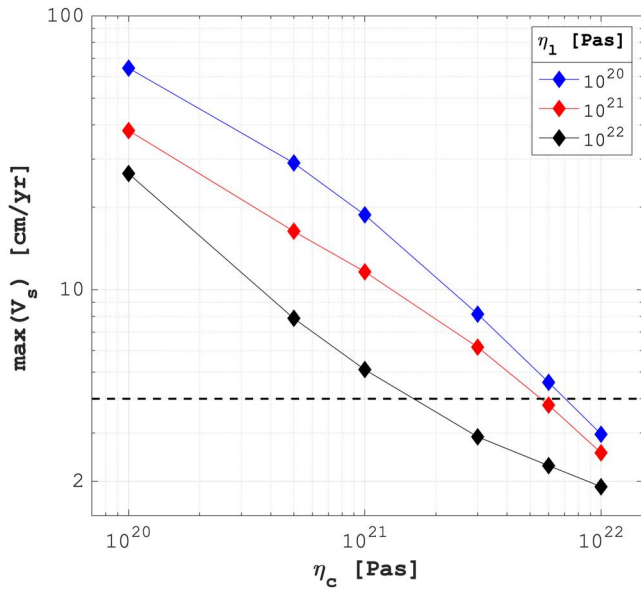
Figure 5. Maximum values of the horizontal velocity, V_s, in the entire crust for models with varying viscosities of the crust and lithospheric mantle. The horizontal axis indicates the crustal viscosity and the color the viscosity of the lithospheric mantle. All results are for models with Earth's curvature and linear viscous flow.

stresses are concentrated in the crust, a phenomenon often referred to as stress amplification (e.g., Bott & Kusznir, 1984).

3.3. Impact of the Crust and Mantle Strength

We present the results of 18 simulations with various viscosities for the crust and lithospheric mantle to determine what crustal viscosities are required to prevent the continental plateau from horizontal flow with unrealistically fast velocities. In our viscous model, the plateau will always flow apart as long as there are lateral variations in GPE, but the horizontal velocities will be negligible if the viscosities are sufficiently large. We consider a model unrealistic if the maximum horizontal velocity exceeds 4 cm/year. The 4 cm/year corresponds approximately to the current indentation velocity of India (e.g., Liang et al., 2013). Such indentation velocity could theoretically balance a spreading velocity of the same magnitude. However, spreading velocities along the northern limit of the Tibetan plateau are smaller than 4 cm/year (e.g., Liang et al., 2013), so that 4 cm/year represents a maximal value of acceptable velocities.

Figure 4 displays the differential stress distribution in cross-sections at 500 km from the edge of the plateau (at position Y = −600 km; see also profile location HP1 in Figure 7). Contours represent horizontal velocities of 4, 10, and 20 cm/year (black, blue and red contours, respectively). In the case of a weak crust (10^{20} Pa · s) and a weak lithospheric mantle (10^{20} Pa · s), stresses are small and velocities are unrealistically large (up to 70 cm/year). An increase of viscosity of either the crust or the lithospheric mantle leads to smaller velocities (Figure 4). A strong lithospheric mantle associated with a weak crust still allows the plateau to spread with unrealistic velocities >20 cm/year (Figure 4c). On the other hand, a strong crust (10^{22} Pa · s) overlying a weak lithospheric mantle (10^{20} Pa · s) exhibits a maximum velocity <4 cm/year (Figure 4g). Moreover, stresses are focusing in the strong layer, which leads to different stress distribution and magnitudes in the crust above a strong lithospheric mantle.

Figure 5 displays the maximum horizontal velocity, $V_s = \sqrt{V_\varphi^2 + V_\theta^2}$, in the entire crust as a function of the crustal viscosity. It shows more clearly the tendency observed in Figure 4, that the larger the crustal viscosity, the slower
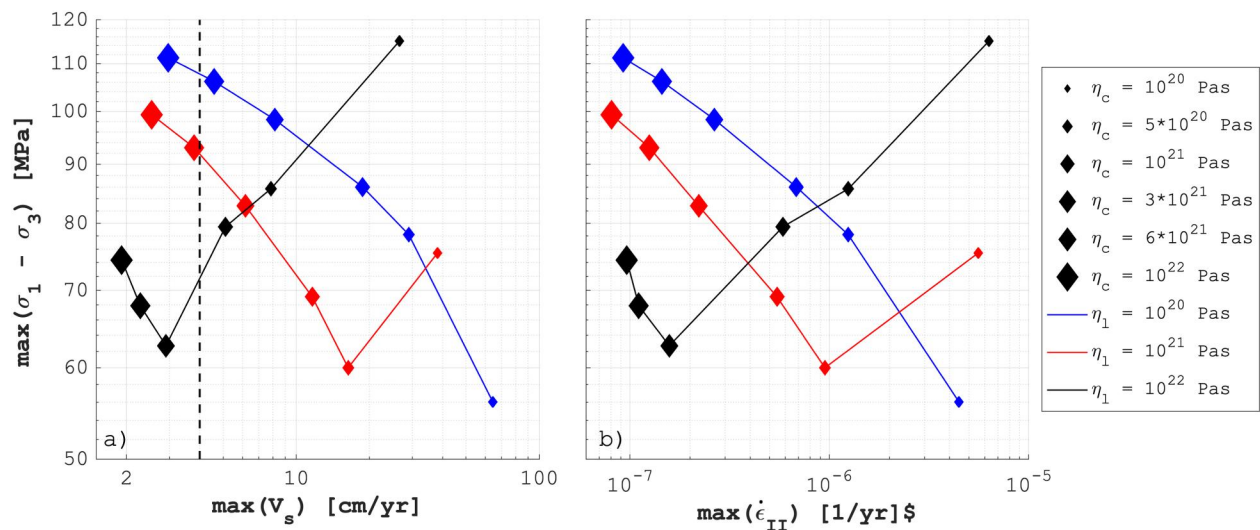

Figure 6. Relation between the maximum crustal differential stress and (a) the maximum horizontal crustal velocity, and (b) the maximum crustal strain rate invariant for models with varying viscosities of the crust and lithospheric mantle. Different crustal (size of markers) and lithospheric mantle (color of markers) viscosities are indicated in the legend of panel (b). All simulations are performed with Earth's curvature and linear viscous flow.
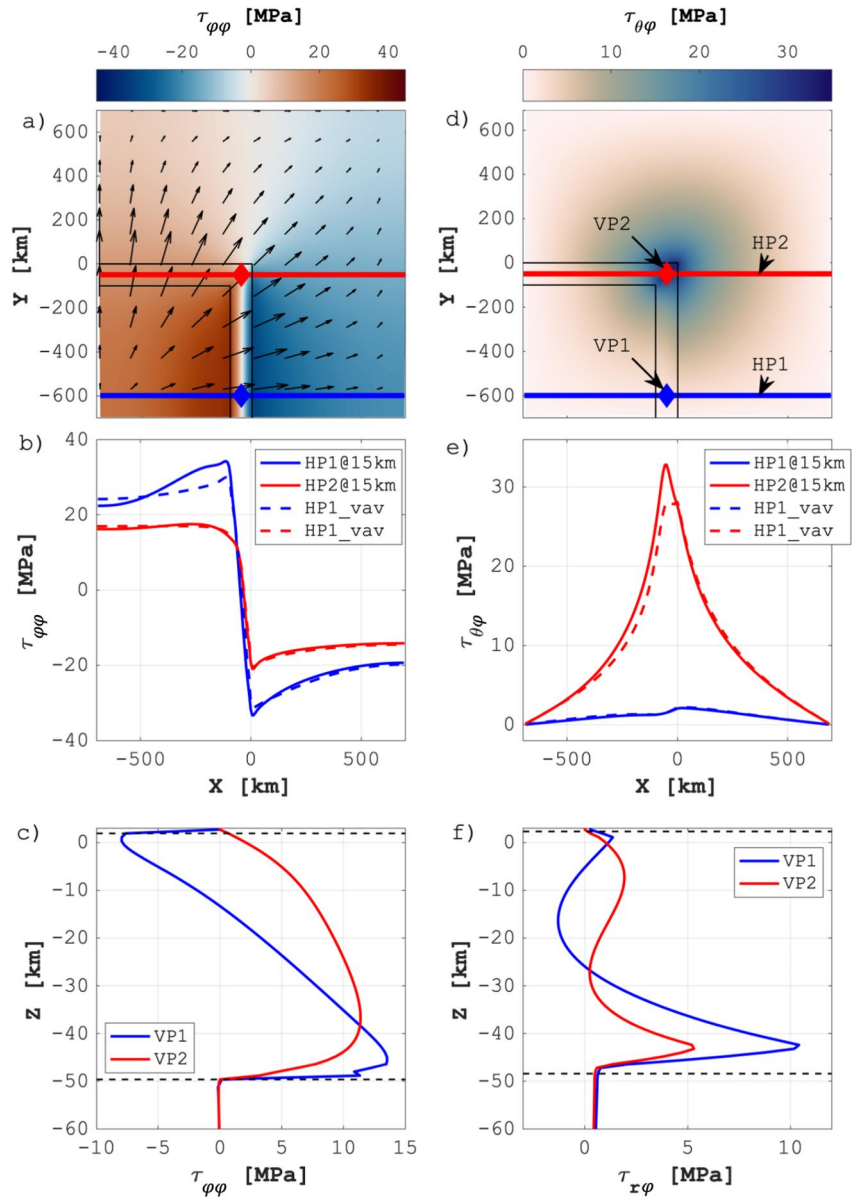
Figure 7. Stress distributions for model SC_WL with Earth's curvature and linear viscous flow. (a, d) Map views. Projection on a flat plane of stresses following the curvature at 15 km depth. (b, e) Horizontal profiles of stresses at 15 km depth and vertically averaged across the crust. Blue line (Profile HP1) is a profile 500 km away from the edge of the plateau and red line (Profile HP2) is inside of the transition between the plateau and the lowland. Panels (a) and (b) display the horizontal deviatoric stress $\tau_{\varphi\varphi}$ and panels (d) and (e) display the horizontal shear stress $\tau_{\theta\varphi}$. Panels (c) and (f) display vertical profiles of horizontal deviatoric stress and vertical shear stress, respectively. The location of the profiles are indicated in panel (d) by VP1 and VP2. The black lines on panels (a) and (d) represent the position of the plateau at the surface and the arrows are the velocity field.

the velocity. For the same crustal viscosities, larger viscosities of the lithospheric mantle cause smaller velocities. Six of our 18 simulations provided velocities smaller than 4 cm/year, all for a crustal viscosity of at least $3 \cdot 10^{21}$ Pa $\cdot$ s.

In addition, Figure 6 presents the relation between the maximum differential stress in the crust and the maximum velocity (Figure 6a) and the maximum strain rate invariant ($\dot{\epsilon}_{II} = \sqrt{0.5\,\dot{\epsilon}_{ij}^2}$) in the crust (Figure 6b). There is no clear correlation between these quantities. Similar stress magnitudes can lead to considerably different velocities or strain rates. For a strong lithospheric mantle, the crustal stress magnitudes do not systematically decrease with
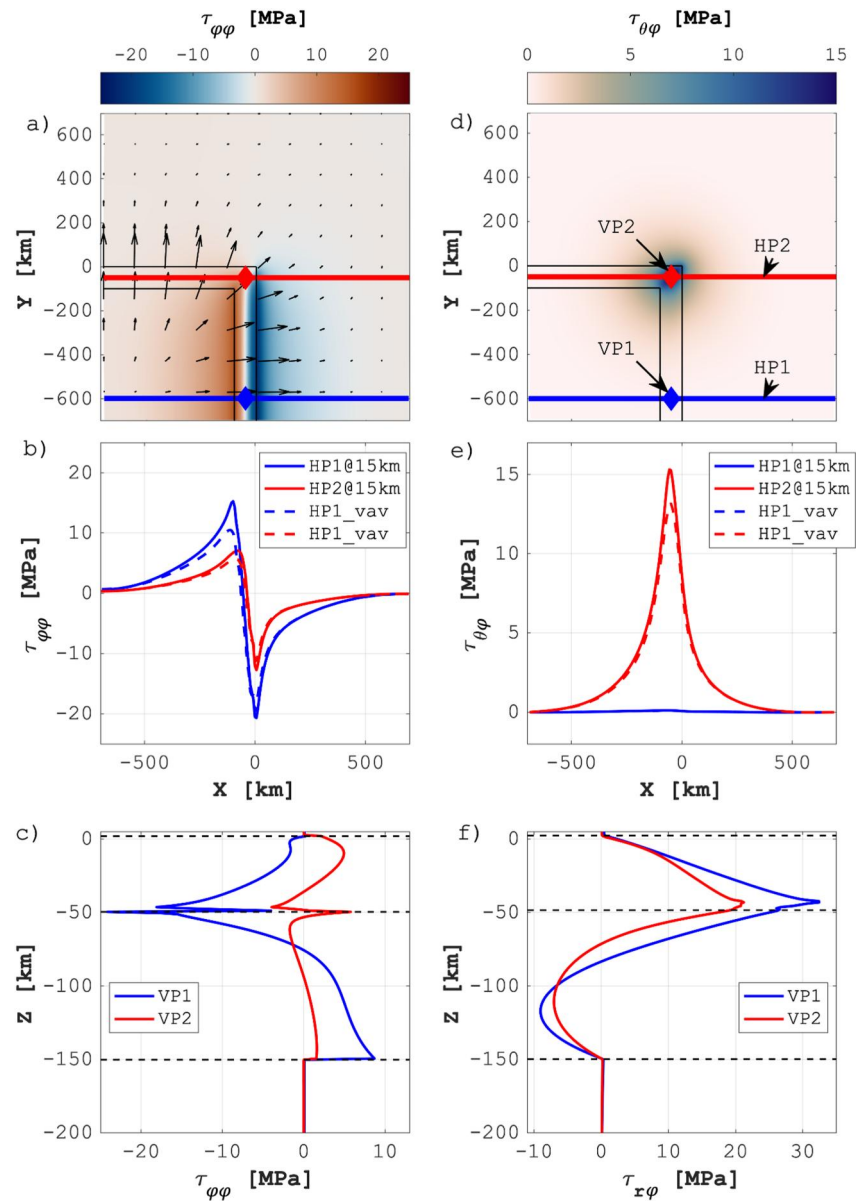
Figure 8. Stress distributions for model IC_SL with Earth's curvature and linear viscous flow. (a, d) Map views. Projection on a flat plane of stresses following the curvature at 15 km depth. (b, e) Horizontal profiles of stresses at 15 km depth and vertically averaged across the crust. Blue line (Profile HP1) is a profile 500 km away from the edge of the plateau and red line (Profile HP2) is inside of the transition between the plateau and the lowland. Panels (a) and (b) display the horizontal deviatoric stress $\tau_{\varphi\varphi}$ and panels (d) and (e) display the horizontal shear stress $\tau_{\theta\varphi}$. Panels (c) and (f) display vertical profiles of horizontal deviatoric stress and vertical shear stress, respectively. The location of the profiles are indicated in panel (d) by VP1 and VP2. The black lines on panels (a) and (d) represent the position of the plateau at the surface and the arrows are the velocity field.

decreasing crustal viscosities (Figure 6a). The reason is that a weaker crust flows faster and hence generates higher strain rates (Figure 6). These higher strain rates cause higher stresses and can balance the decrease in viscosity to maintain similar stress magnitudes. Magnitudes of stress are hence not a reliable proxy for lithospheric strength which is governed by the effective viscosity.

3.4. Impact of a Rectangular Corner

For model SC_WL, Figure 7a displays the deviatoric normal stress at 15 km depth in map view. The horizontal velocities indicate that the plateau flows apart (Figure 7a). Laterally far away from the corner, the horizontal
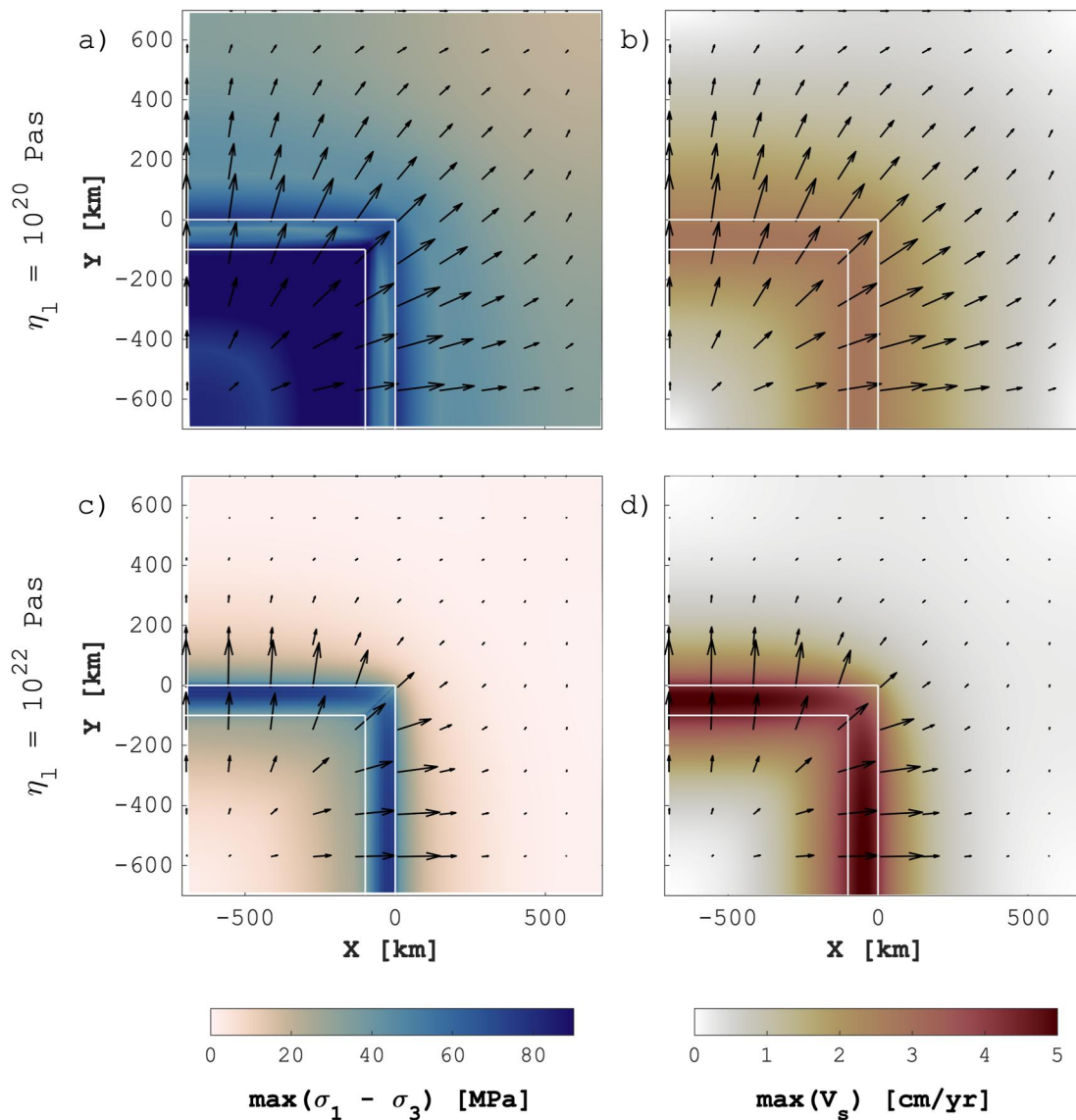
Figure 9. Map views showing the lateral distribution of maximum differential stress and horizontal velocities for models SC_WL and IC_SL. Maximum value in the crust at every horizontal position of differential stress (a, c), and horizontal velocity (b, d). Panels (a) and (b) display the simulation with the model SC_WL, and panels (c) and (d) show the simulation with the model IC_SL. The white lines represent the position of the plateau at the surface and the arrows indicate the velocity field. These simulations are done using the Earth's curvature and linear viscous flow.

velocities have a direction that is orthogonal to the plateau boundary in map view (Figure 7a). Along the plateau boundary in map view, the direction of the horizontal velocities becomes less orthogonal the closer the velocities are to the corner (Figure 7a). Due to the rectangular shape of the corner in map view, the horizontal velocities have an orientation of 45° at the corner point at the position X = 0 [km] and Y = 0 [km] (Figure 7a). The horizontal deviatoric normal stresses away from the corner and orthogonal to the plateau boundary are highest around the plateau boundary, for example, for $\tau_{\varphi\varphi}$ along profile HP1 (Figure 7b). Magnitudes of $\tau_{\varphi\varphi}$ decrease toward the corner (profile HP2 in Figure 7a). This is visible in Figure 7b which shows about 10 MPa difference in absolute stress magnitudes between the two profiles. For comparison, we show two profiles for two stress magnitudes: a profile of the stress at 15 km depth (solid line in Figures 7b and 7e) and a profile for the corresponding stress that is vertically averaged across the crust (dashed lines). Both stress profiles are similar (Figure 7b).

Figure 7d displays the horizontal shear stress at 15 km depth in map view. Shear stresses are significant only in the corner region with magnitudes of up to more than 30 MPa. The shear stresses increase nonlinearly toward the
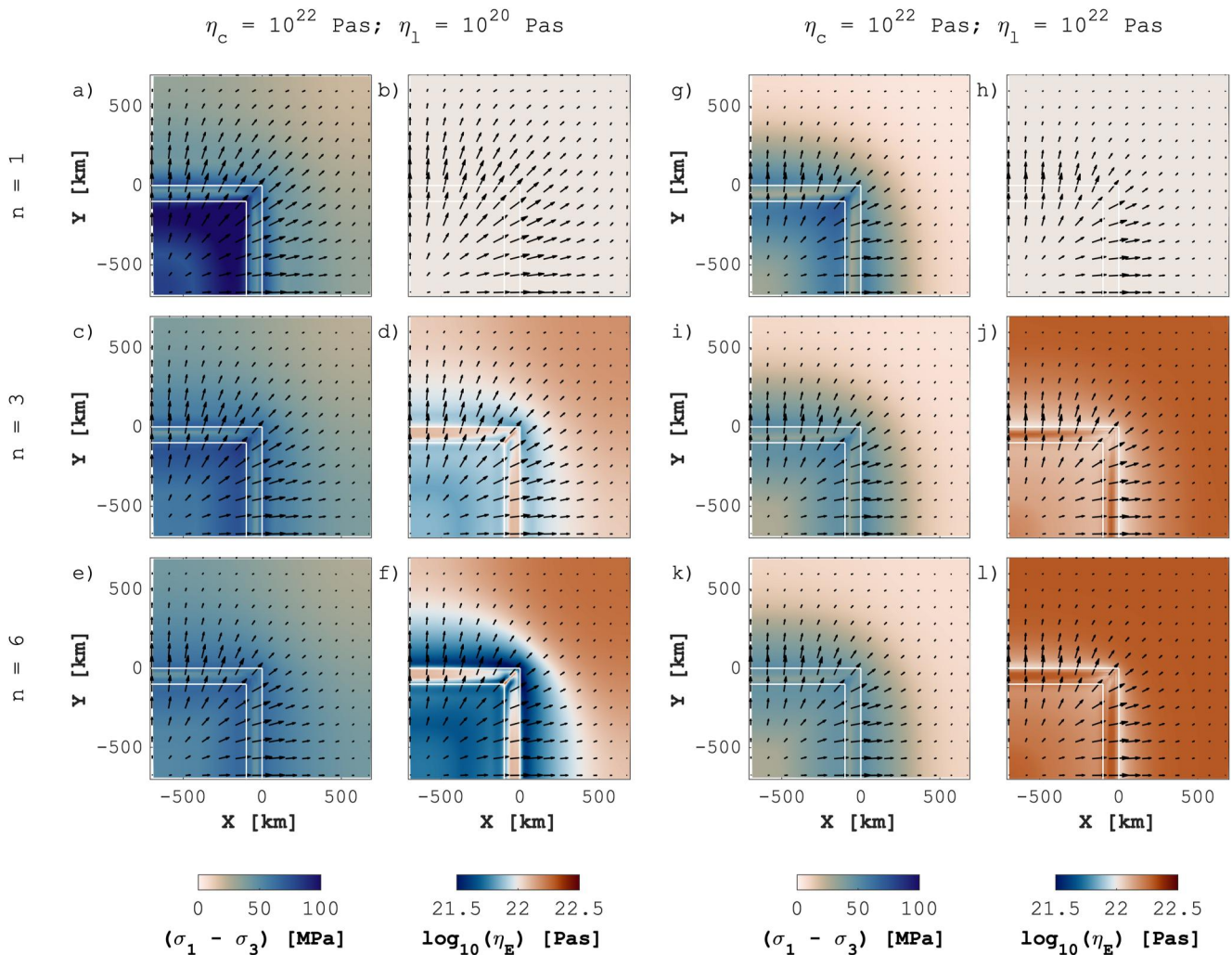
Figure 10. Map views of maximum values of crustal differential stress and effective viscosity for two simulations with power-law viscous flow with different stress exponents n. Panels (a)–(f) display results for a simulation with a strong crust (10^{22} Pa · s) and a weak lithospheric mantle (10^{20} Pa · s). Panels (g)–(l) display results for a simulation with a strong crust (10^{22} Pa · s) and a strong lithospheric mantle (10^{22} Pa · s). Panels (a), (c), and (e), and panels (g), (i), and (k) display the differential stress. Panels (b), (d), and (f), and panels (h), (j), and (l) display the effective viscosity. The corresponding stress exponent n is indicated on the left of each of the three rows of panels. All models are with the Earth's curvature.

corner, indicated by the concave-upward curve of shear stress versus distance (Figure 7e). Away from the corner region, horizontal shear stresses become negligible (Figures 7d and 7e).

We also present representative vertical profiles of normal deviatoric stress and vertical shear stress (Figures 7c and 7f). Both stresses show a significant vertical variation across the crust. Vertical shear stresses are essentially zero at the top and bottom of the crust but vary considerably vertically (Figure 7f). Maximum values of vertical shear stresses reach ≈10 MPa.

As for model SC_WL (Figure 7), we present the same map views and stress profiles for model IC_SL (Figure 8). Compared to model SC_WL, in model IC_SL the crustal stress magnitudes are smaller, normal deviatoric stresses reach up to only 20 MPa along profile HP1 and shear stresses reach 30 MPa in the corner region (profile HP2). However, the general crustal stress pattern is the same in both models, with decreasing normal deviatoric stresses and larger shear stresses toward the corner. The vertical profile of the vertical shear stresses shows that shear stresses are largest at the crust-mantle boundary and that maximum values are ≈35 MPa (Figure 8f).

Figure 9 displays map views of the maximum crustal differential stress and horizontal crustal velocities at each horizontal position. For each horizontal location, we select the largest crustal value along the vertical profile at
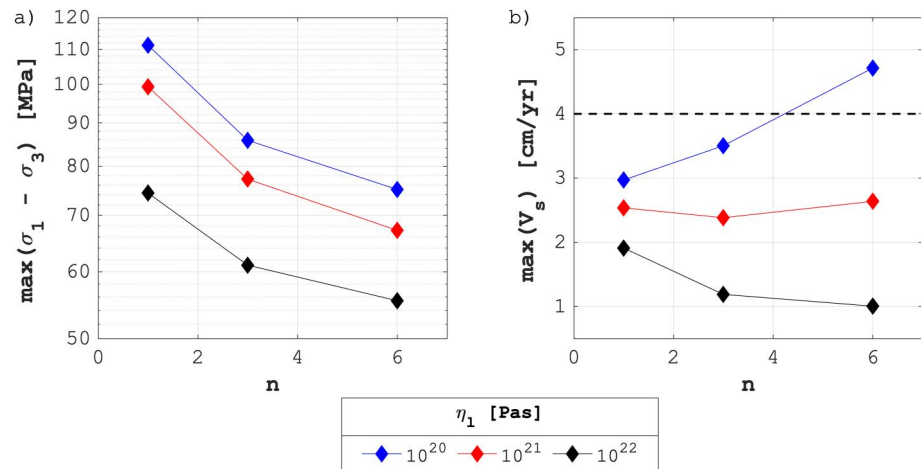
Figure 11. Variation of the maximum (a) differential stress and (b) horizontal velocity of the entire crust with increasing power-law stress exponent n. All simulations are with the Earth's curvature, a crustal viscosity value of $\eta = 10^{22}$ Pa · s and with $\tau_C = 24$ MPa.

this location. For model SC_WL (Figures 9a and 9b), differential stresses are highest in the plateau and maximum values are $\approx$100 MPa (Figure 9a). Conversely, for model IC_SL (Figures 9c and 9d), differential stresses are largest along the transition zone (Figure 9c). Inside the plateau, differential stresses are smaller than ca. 40 MPa. The comparison of model SC_WL with IC_SL shows that the viscosity ratio between the crust and lithospheric mantle has a major impact on the magnitude and distribution of crustal differential stress.

The distribution of maximum crustal horizontal velocities is also different for models SC_WL and IC_SL (Figures 9b and 9d). For model SC_WL, the velocity magnitudes vary less across the model domain compared to model IC_SL for which maximum magnitudes are localized along the transition zone. The magnitudes of the spreading velocities are lager for model IC_SL compared to SC_WL.

In map view, the magnitudes of differential stress and horizontal velocities do not vary significantly along the transition zone for both simulations with strong and intermediate crust (Figure 9). In other words, only the directions change along the transition zone, but the magnitudes of stress and horizontal velocity change insignificantly. Far away from the corner region, the magnitude contours of normal deviatoric stresses run parallel to the plateau edge, and shear stresses are negligible. This suggests that far away from the corner region there are no significant 3D features in the stress field. However, it is important to take into account the 3D characteristics of the plateau close to the corner region where horizontal shear stresses are significant.

3.5. Impact of a Stress-Dependent Power-Law Flow Law

In our combined linear and power-law viscous flow law, we need to specify the characteristic stress that controls the transition from linear viscous (e.g., diffusion creep) to power-law viscous flow (e.g., dislocation creep). We define τ_C at 24 MPa. As a consequence, effective viscosity decreases when stresses are larger than τ_C and increases when stresses are smaller. If we refer in this sub-section to a viscosity value applied in a model, then we refer to the linear viscosity, η, used in Equation 11 for the effective viscosity, η_E.

Figure 10 displays map views of differential stress and effective viscosity. For both quantities, we plot the maximum value of the crust at each horizontal position. Results for a strong crust (10^{22} Pa · s) and a weak lithospheric mantle (10^{20} Pa · s), model SC_WL, show that stress magnitudes decrease and the stress distribution gets smoother as the power-law exponent increases (Figures 10a–10f). Also, the effective viscosity varies from a constant value (linear viscous) to more and more variable values (Figures 10b, 10d, and 10f). Differences in effective viscosity reach up to one order of magnitude for n = 6 (Figure 10f). In the plateau, where stresses are high, the effective viscosity for n = 3 and 6 is smaller compared to the linear viscous one. However, far away from the plateau the stresses are smaller than τ_C which leads to an increase in effective viscosity.
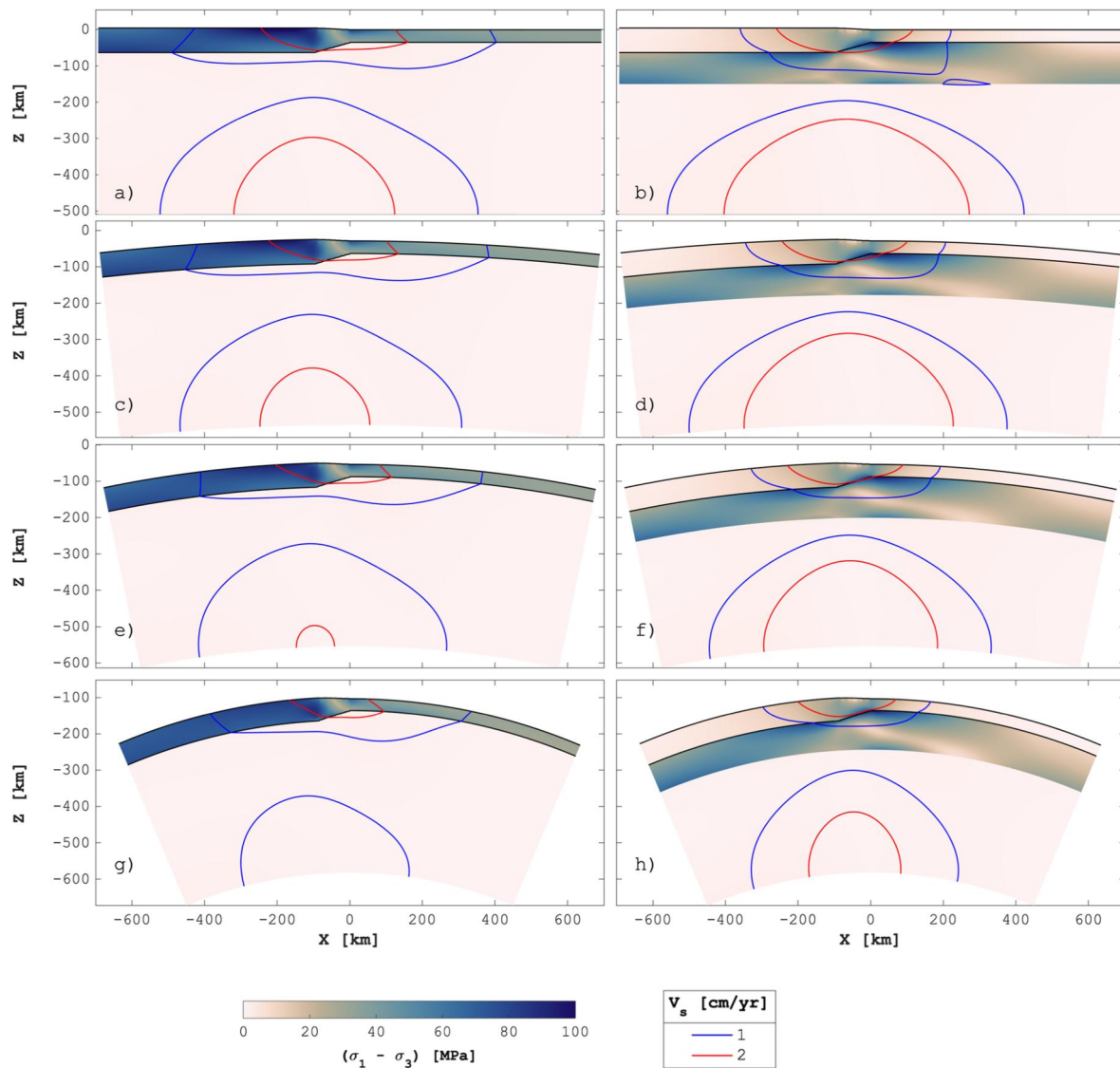
Figure 12. Cross-sections at 500 km from the edge of the plateau ($Y = -600$ km) showing the differential stress. Different curvatures corresponding to (a, b) negligible curvature, (c, d) the Earth, (e, f) Mars, and (g, h) the Moon are displayed. Panels (a), (c), (e), and (g) display results for model SC_WL, and panels (b), (d), (f), and (h) display results for model IC_SL. The contours mark horizontal velocities of 2 cm/year (red) and 1 cm/year (blue). All results are for linear viscous flow.

Results for a strong crust (10^{22} Pa · s) and a strong lithospheric mantle (10^{22} Pa · s) show small differences in the differential stress distribution for increasing values of n (Figures 10g, 10i, and 10k). The reason is that crustal deviatoric stresses do not significantly exceed the characteristic stress. Hence, the effective viscosity increases nearly everywhere, except in the transition zone between plateau and lowlands (Figures 10h, 10j, and 10l).

Figure 11 presents the maximum differential stress and horizontal velocity of the entire crust as a function of the power-law exponent. For all lithospheric mantle viscosities, the maximum differential stress decreases as the power-law exponent increases (Figure 11a). For example, for the model with a lithospheric mantle viscosity of $\eta_l = 10^{21}$ Pa · s, the maximum differential stress decreases from ≈ 100 to ≈ 67 MPa when n increases from 1 to 6 (red curve in Figure 11a). For lithospheric mantle viscosities between $\eta_l = 10^{21}$ Pa · s and $\eta_l = 10^{22}$ Pa · s, the maximum velocities vary little when n increases (Figure 11b). The velocity increases with increasing n for a lithospheric mantle viscosity of $\eta_l = 10^{20}$ Pa · s because in this model the crustal stresses are largest and the stress weakening effect due to power-law flow is largest.
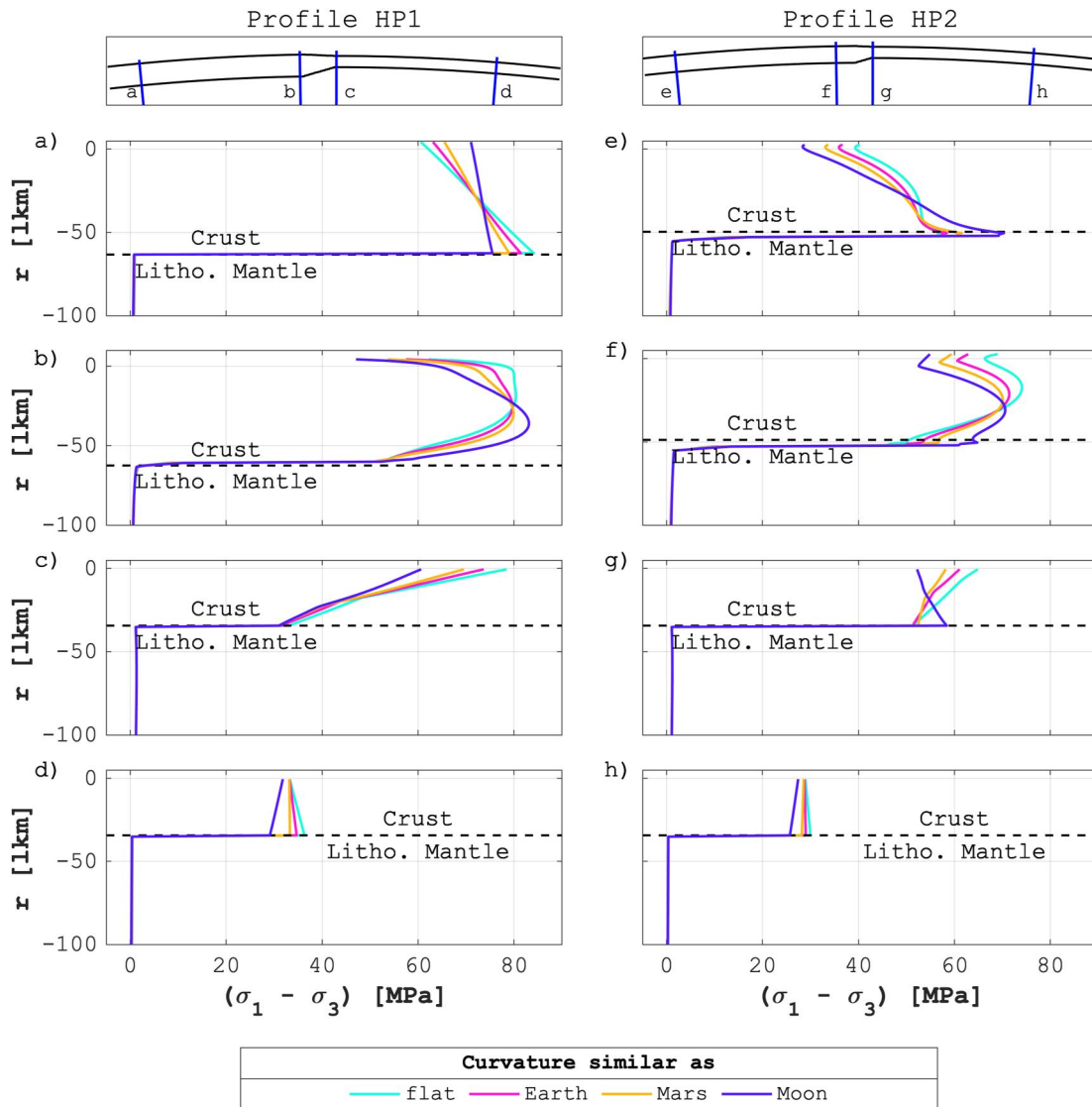
Figure 13. Representative vertical profiles of differential stress, $(\sigma_1 - \sigma_3)$, in radial direction for model SC_WL with different curvatures. In panels (a)–(d) the profiles are taken at 500 km from the edge of the plateau along the *Y*-axis (Profile HP1 in Figure 7) and their position in direction *X* are (a) 500 km from the edge of the plateau, (b) 5 km from the edge, (c) 5 km after lowland started, and (d) 500 km after the end of the transition between the plateau and the lowland (positions are indicated in the top panel). In panels (e)–(h), profiles are taken in the middle of the transition zone between the plateau and its surrounding lowlands (Profile HP2 in Figure 7) and are distributed the same way as the left side along direction *X* (positions displayed in the top panel). The different lines represent different curvatures (see legend) and the dashed line marks the limit between the crust and the lithospheric mantle. All of these simulations are done with the model SC_WL. All results are for linear viscous flow.

The presented results show the general impacts of a power-law viscous flow on the magnitudes of stress and spreading velocities. Specific results depend on the applied value of τ_C but a systematic analysis of the impact of different values of τ_C is beyond the scope of our study.

3.6. Impact of the Curvature

To quantify the impact of curvature on the stresses in and around the continental plateau, we modify the radius of the spherical coordinate system without changing the geometry of the model domain. In other words, the arc length of the crust stays constant, and as the radius of the sphere decreases the central angle increases. Hence, the curvature of the domain increases.
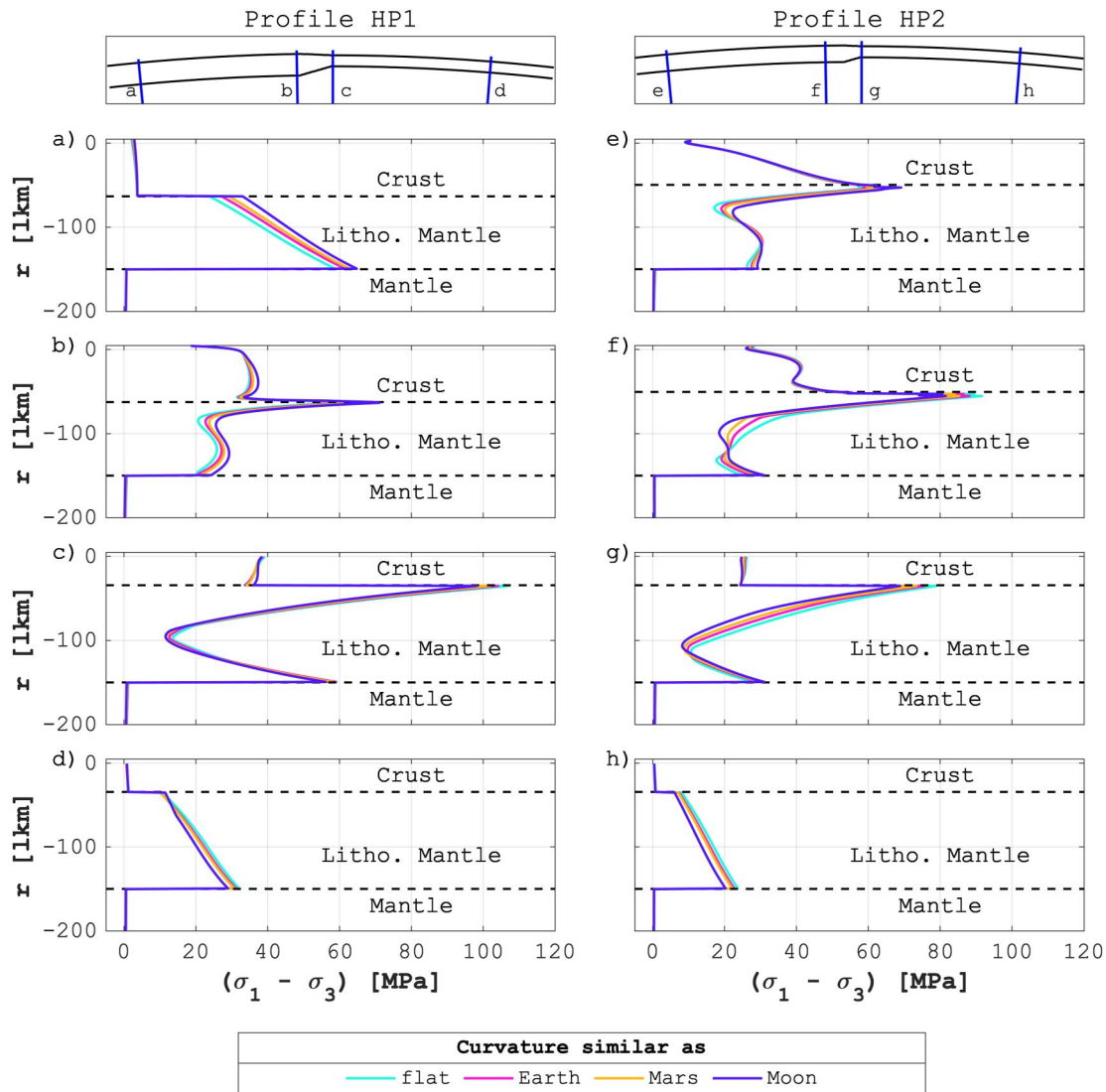
Figure 14. Representative vertical profiles of differential stress, $(\sigma_1 - \sigma_3)$, in radial direction for model IC_SL with different curvatures. In panels (a)–(d) the profiles are taken at 500 km from the edge of the plateau along the *Y*-axis (Profile HP1 in Figure 7) and their position in direction *X* are (a) 500 km from the edge of the plateau, (b) 5 km from the edge, (c) 5 km after lowland started, and (d) 500 km after the end of the transition between the plateau and the lowland (positions are indicated in the top panel). In panels (e)–(h), profiles are taken in the middle of the transition zone between the plateau and its surrounding lowlands (Profile HP2 in Figure 7) and are distributed the same way as the left side along direction *X* (positions displayed in the top panel). The different lines represent different curvatures (see legend) and the dashed line marks the limit between the crust, the lithospheric mantle and the mantle. All of these simulations are done with the model IC_SL. All results are for linear viscous flow.

Figure 12 displays the differential stress $(\sigma_1 - \sigma_3)$ for four different curvatures using a radius of curvature corresponding to a very large radius to generate essentially no curvature ($6,371 \cdot 10^3$ km), the radius of the Earth (6,371 km), of Mars (3,390 km), and of the Moon (1,737 km). We use these radii for Mars and the Moon simply as examples to test the impact of increasing curvature. All four curvatures have been tested with model SC_WL and model IC_SL. To first order, we do not see any significant effect of curvature on the stresses and on the horizontal velocities. Representative horizontal velocity magnitudes are indicated by the contour lines.

Eight vertical profiles of differential stresses, from two horizontal sections, are compared in Figure 13 for model SC_WL and in Figure 14 for model IC_SL. The different curvatures are displayed for each vertical profile. There are two sets with four vertical profiles each. The two sets show vertical profiles that belong to two horizontal profiles: Profile HP1 (Figures 13a–13d and 14a–14d) is located far away from the corner region and its location is displayed in Figure 7d. Profile HP2 (Figures 13e–13h and 14e–14h) is located inside the transition zone between
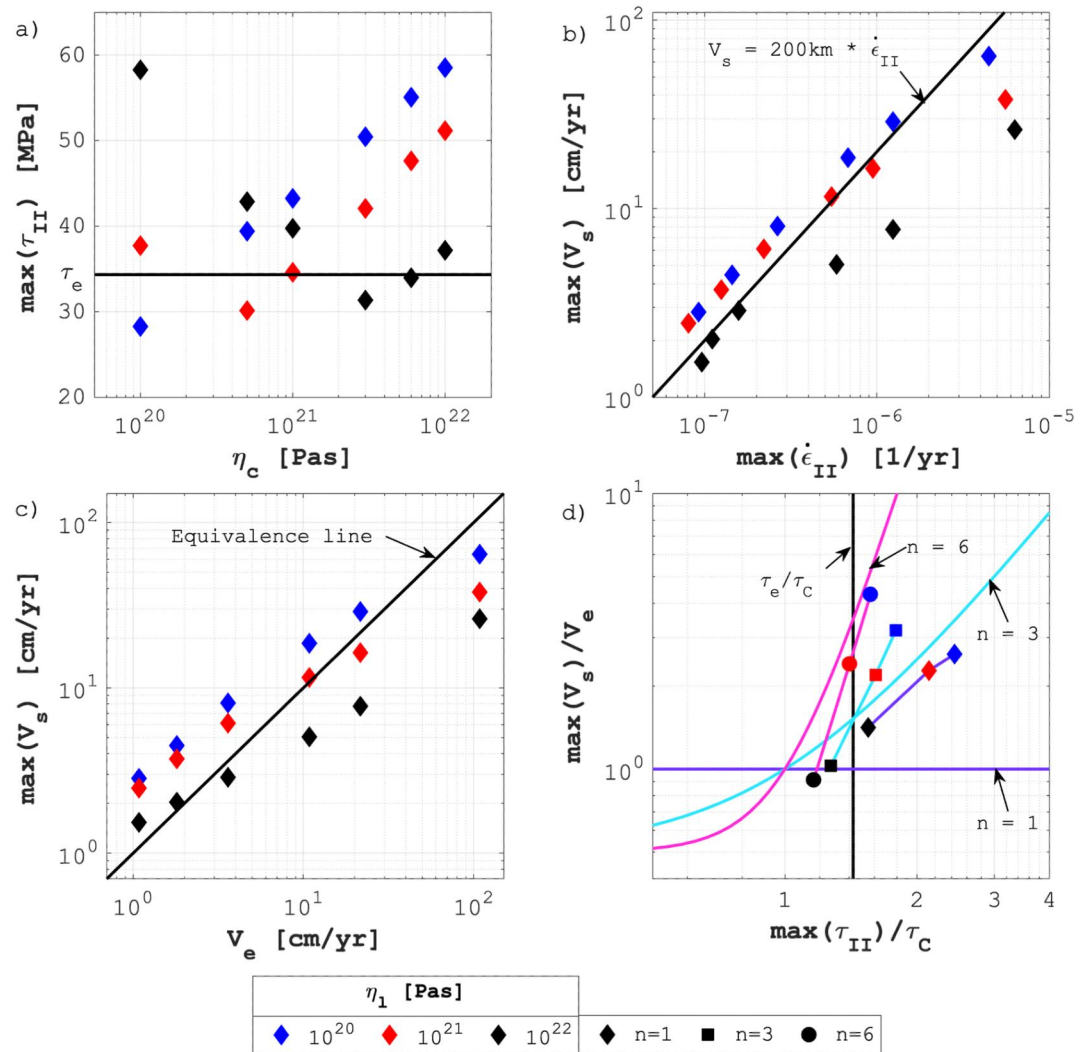
Figure 15. Comparison of analytical estimates with numerical results. The legend at the bottom of the figure indicates the values used in the numerical calculations. (a) Maximum value of τ_{II} in the crust from numerical calculation versus crustal viscosity, η_c. The horizontal black line indicates the analytical estimate for the deviatoric stress, τ_e. (b) Maximum value of crustal horizontal velocity, V_s, versus the maximum value of $\dot{\epsilon}_{II}$. The black line indicates the applied analytical estimate for the relation between velocity, V_e, and strain rate, $\dot{\epsilon}$. (c) Comparison of numerical velocity, V_s, with analytical estimate, V_e. The black line indicates the equivalence between numerical and analytical velocities. (d) Dimensionless horizontal velocity versus the stress ratio that controls the stress-dependent effective viscosity. The solid lines indicate the analytical velocity estimate for different values of n (see Equation 10).

the plateau and the lowland and displayed in Figure 7d. For model SC_WL, the impact of the different curvatures on the differential stress profile is generally minor. There is an average difference of 0.15 MPa between the flat simulation and the one with the Earth radius and a maximum difference of less than 10 MPa. Hence, for the case of a 3D model applied to Earth, a flat (Cartesian) model provides stresses that are close to stresses resulting from a model considering the Earth's curvature. For a curvature corresponding to the radius of the Moon, some vertical profiles show opposite trends of stress profiles compared to models with a radius corresponding to Earth (Figures 13d, 13g, and 13h). For example, in the vertical profile in the lowland close to the transition zone and the plateau corner, the differential stresses in the crust increase with depth for the radius of the Moon, but decrease with depth for all other models with larger radii (Figure 13g). However, the magnitudes of the differential stresses are similar.

For model IC_SL, there are only minor differences between the differential stress profiles for a model with flat geometry and with Earth's, Mars' and Moon's curvature (Figure 14).

3.7. Scaling Estimates of Stress and Velocity

For all the numerical calculations with linear viscous flow, we compare the maximum numerical value of τ_{II} in the crust with the analytical estimate τ_e since both stress magnitudes represent deviatoric stresses (Figure 15a). The estimated value of τ_e is ≈ 34 MPa for the applied model configuration and this value predicts the numerical values of τ_{II} accurately within a factor of ≈ 2. The comparison shows that τ_e tends to provide a lower bound for the numerical stress magnitudes (Figure 15a). The numerical results also show that stress magnitudes depend only slightly on the crustal viscosity. While the viscosity of both the crust and lithospheric mantle varies by two orders of magnitude, the stress magnitudes only vary within a factor of less than ≈ 2 which supports the analytical estimate of τ_e that is estimated independently of the viscosity.

The numerical results show that there is an approximately linear correlation between the maximum horizontal velocity, V_s, and the maximum strain rate invariant, $\dot{\epsilon}_{II}$ (Figure 15b). We have assumed such linear relation in Equation 6 to derive an analytical estimate for the velocity. A length scale, L, that captures the observed relation between the numerical velocities and strain rates is ≈ 200 km. The 200 km corresponds to twice the width of the transition zone. For the analytical estimate of the velocity, V_e, we hence use $L = 200$ km (see Equation 7).

The comparison between the maximum value of the numerical velocity, V_s, and the corresponding analytical estimate, V_e, shows that V_e can accurately predict the velocities within a factor of ≈ 3 (Figure 15c). Such accuracy of V_e is remarkable because in the numerical calculations both η_c and η_l vary between 10^{20} and 10^{22} Pa $\cdot$ s, and the numerical calculations consider all end-member combinations of η_c and η_l (Figure 4).

We made calculations with a stress-dependent viscosity only for a crustal linear viscosity of 10^{22} Pa $\cdot$ s. The applied value of τ_C is 24 MPa. The estimated value of $\tau_e/\tau_C \approx 1.4$ (Figure 15d). For simulations with $n = 6$, the estimated value of τ_e/τ_C is closest to the numerical values of $\max(\tau_{II})/\tau_C$ while for simulations with $n = 1$ the value of τ_e/τ_C underestimates the numerical values (Figure 15d). Simulations with $n = 6$ show the smallest variation in $\max(\tau_{II})/\tau_C$ (from ≈ 1.2 to ≈ 1.6) but the largest variation in $\max(V_s)/V_e$ (from ≈ 0.9 to ≈ 4.2) which is consistent with the analytical estimate (Figure 15d). Conversely, simulations with $n = 1$ show the largest variation in $\max(\tau_{II})/\tau_C$ (from ≈ 1.6 to ≈ 2.4) but the smallest variation in $\max(V_s)/V_e$ (from ≈ 1.3 to ≈ 2.6). Simulations with $n = 1$ should theoretically not vary with varying $\max(\tau_{II})/\tau_C$ and the velocity variations are due to differences between $\max(\tau_{II})$ and τ_e causing the inaccuracy in the velocity prediction.

4. Discussion

4.1. Viscous Deformation of the Lithosphere

For simplicity, we consider only a linear and a power-law viscous deformation of the lithosphere and neglect elastic and frictional-plastic deformation. We use viscosities between 10^{20} and 10^{22} Pa $\cdot$ s. Typical values of the elastic shear modulus for lithospheric rocks are $\approx 3 \cdot 10^{10}$ Pa (e.g., Dziewonski & Anderson, 1981). The characteristic Maxwell viscoelastic stress relaxation time is given by the ratio of viscosity to shear modulus (e.g., Turcotte & Schubert, 2014). The duration of the relaxation of elastic stresses in a viscoelastic material is approximated by the Maxwell time. For the applied viscosities between 10^{20} and 10^{22} Pa $\cdot$ s, and a typical shear modulus of $\approx 3 \cdot 10^{10}$ Pa, the Maxwell time is between 100 and 10,000 years. Since we are interested in the long-term stability of continental plateaus, say >1 Myr, it is justifiable to neglect elastic effects in our application because elastic stresses are relaxed after $\approx 10,000$ years for our model configuration.

The maximum differential stresses in our model are ≈ 110 MPa (Figure 6), and maximum differential stresses close to the surface are <80 MPa (Figure 13). Frictional-plastic yield stresses in the continental crust are >80 MPa already below a few kilometers of depth (e.g., Kohlstedt et al., 1995; Townend & Zoback, 2000). Therefore, in our model, only the uppermost few kilometers of the continental crust would be affected by frictional-plastic deformation, because most of our model crust deeper than a few kilometers exhibits differential stresses below typical yield stresses. Furthermore, differential stresses in the lithospheric mantle in all the performed models are also <100 MPa, and stresses are, hence, below the yield stress in the lithospheric mantle (Figure 4). The

application of an effectively viscous deformation behavior of the lithosphere is, hence, justifiable for our model and our modeling objectives.

4.2. Rheological Layering; Crustal and Lithospheric Mantle Viscosities

We consider in our model three rock layers that can have different viscosities, namely η_c, η_l, and η_m (Figure 2c). If all three viscosities are identical, $\eta_c = \eta_l = \eta_m$, then the viscosity distribution would correspond to the constant viscosity of the thin viscous sheet model. The thin viscous sheet model was applied to investigate the deformation of the continental lithosphere in many regions worldwide, such as Tibet, New Zealand, the Apennines, the Andes or the Aegean (D'Agostino et al., 2014; England & McKenzie, 1982; England et al., 2016; Flesch et al., 2001; Hirschberg et al., 2019; Lamb, 2000). Many studies estimated the average viscosity of the lithosphere, mostly in combination with the analysis of GPS measurements and strain rate estimates, between 10^{21} and 10^{23} Pa · s (D'Agostino et al., 2014; England & Molnar, 1997; England et al., 2016; Flesch et al., 2001; Hirschberg et al., 2019; Lamb, 2000). These previous studies support the viscosity values applied here. A model with $\eta_c = \eta_l \ll \eta_m$ would correspond to a rheological scenario of a gravity current over a rigid base. Such a scenario was used, for example, to investigate crustal flow related to the India-Asia collision (e.g., Copley & McKenzie, 2007). A model with $\eta_c \gg \eta_l \ll \eta_m$ would correspond to a rheological scenario of channel flow that was applied to study lower crustal flow in and around the Tibetan plateau (e.g., Clark & Royden, 2000).

Our results show that the ratio of crustal to lithospheric mantle viscosity has a significant impact on the stress distribution in the lithosphere. For the estimation of crustal stresses in regions with significant lateral variation of GPE, it is therefore essential to apply models that can consider different viscosities in the crust and lithospheric mantle. Thin viscous sheet models with constant viscosity are not well suited to estimate crustal stress magnitudes in such regions.

Our results show that a strong lithospheric mantle alone is not sufficient to support the Tibetan plateau. The crust must also have significant strength to prohibit an unrealistically fast horizontal dilatation of the plateau. For the strongest lithospheric mantle in our model we apply a viscosity of 10^{22} Pa · s. Below the crust-mantle boundary (Moho), effective viscosities of the lithospheric mantle may be slightly higher than 10^{22} Pa · s, especially below the lowland due to colder Moho temperatures compared to the thicker plateau (e.g., Hirth & Kohlstedt, 2003; Mei et al., 2010). However, since we apply a constant viscosity in the lithospheric mantle, this viscosity represents a vertically averaged viscosity. We apply the viscosity of 10^{22} Pa · s for the lithospheric mantle down to a depth of 150 km. In such depth, and for the correspondingly hotter temperatures, the viscosity of the lithospheric mantle is smaller than 10^{22} Pa · s (e.g., England & Molnar, 2015; Hirth & Kohlstedt, 2003; Mei et al., 2010). Therefore, the modeled lithospheric mantle with a constant viscosity of 10^{22} Pa · s represents a strong lithospheric mantle compared to more realistic vertical viscosity variations based on experimentally derived flow laws.

We consider a crust that causes horizontal velocities larger than 4 cm/year as mechanically too weak to support the Tibetan plateau. We chose 4 cm/year because this value is like the present-day indentation velocity of India (e.g., Liang et al., 2013). Our results show that the vertically averaged viscosity of the crust must be at least $3 \cdot 10^{21}$ Pa · s or larger so that spreading velocities in the crust are everywhere smaller than 4 cm/year. This average viscosity value is quite large considering the larger-than-normal thickness of the crust forming continental plateaus (≈ 70 km in the Tibetan plateau) and its associated large vertical temperature variation. For example, the upper limit for lower crustal viscosities, resulting from geodetic estimates (e.g., Thatcher & Pollitz, 2008), is $\approx 3 \cdot 10^{21}$ Pa · s, and many studies suggest lower crustal viscosities to range between 10^{18} and $3 \cdot 10^{20}$ Pa · s (e.g., Doin et al., 2015; England et al., 2013; Shi et al., 2015). If such low-viscosity estimates for the continental lower crust are accurate, then our results imply that the average, effective viscosity of the upper crust must be considerably larger than $3 \cdot 10^{21}$ Pa · s in order to support the topographic variation between the Tibetan plateau and surrounding lowland for geological time scales $> \approx 1$ Myr.

4.3. Shear Stresses and Corner

The crustal shear stresses vary significantly in both the horizontal and vertical directions (Figures 7 and 8). In the corner region of the plateau, the magnitudes of the horizontal shear stresses are even larger than the absolute magnitudes of the horizontal deviatoric normal stresses (Figures 7 and 8). Conversely, away from the corner region, the horizontal shear stresses are essentially negligible (Figures 7 and 8).

The vertical shear stresses vary significantly in the vertical direction at the transition zone. For a strong crust and weak lithospheric mantle (SC_WL), the shear stresses have a maximum absolute value of ≈10 MPa (Figures 7c and 7f). For an intermediate strong crust and strong lithospheric mantle (IC_SL), the shear stresses reach a maximum absolute value of ≈30 MPa at the base of the crust (Figure 8f). The existence of such shear stresses has important implications for thin viscous sheet models because in these models the vertical shear stresses are considered to be zero (e.g., England & McKenzie, 1982; Schmalholz et al., 2014). Such thin viscous sheet approximations, that neglect vertical shear stresses, are often applied to quantify the global lithospheric stress field (e.g., Coblentz et al., 1994; Ghosh et al., 2009; Lithgow-Bertelloni & Guynn, 2004) or the stresses and forces associated with large-scale tectonic plate motion (e.g., Ghosh et al., 2006; Warners-Ruckstuhl et al., 2012, 2013). These models provide first-order accurate magnitudes of large-scale lithospheric stresses. Our results indicate that care should be taken when interpreting such stress fields in regions with significant lateral GPE variations because in these regions vertical shear stresses can be significant and can have a first-order impact on stress magnitudes. The vertical variation of the vertical shear stress is associated with a vertical variation of the horizontal deviatoric normal stresses (Figures 7c, 7f, 8c, and 8f). The horizontal deviatoric normal stress changes its sign with depth (Figures 7c and 8c) which is typically resulting from bending of the lithosphere around the transition zone (Schmalholz et al., 2019). Medvedev and Podladchikov (1999) have derived an extended thin viscous sheet model that considers vertical shear stresses. However, this extended thin sheet model can also not resolve differences in crustal and lithospheric mantle viscosities.

2D lithospheric models configured for vertical cross-sections provide accurate stress fields if the cross-section has a distance from a corner region of at least a few hundred kilometers. If the modeled cross-section is closer, then horizontal shear stresses are significant (Figures 7 and 8). The modeled 2D stress field can be, hence, considerably inaccurate because it does not take into account these horizontal shear stresses.

4.4. Power-Law Viscous Flow Law and τ_C

We apply only one particular value of τ_C to test the first-order impact of power-law viscous flow on the crustal stress and extensional velocity. If a particular flow law, which is determined by laboratory rock deformation experiments, should be applied, then the value of τ_C can be calculated for a given pressure, temperature or grain size (Macherel, Podladchikov, et al., 2023). For example, for feldspar (wet anorthite), $\tau_C \approx 24$ MPa for a temperature of ≈600°C and a grain size of ≈0.5 mm (Macherel, Podladchikov, et al., 2023).

Alternatively, one could consider the value of τ_C as an effective parameter that needs to be estimated by fitting numerical results to observations. For example, the value of an effective stress exponent n can represent the power-law viscous behavior of the vertically averaged lithospheric viscosity (e.g., Houseman & England, 1986). Houseman and England (1986) estimated that the value of the effective n should be larger than 3 to fit thin viscous sheet results with observations and data for the Tibetan plateau. Similarly, bounds on the value of an effective τ_C might be estimated by comparing model results with observations such as GPS measurements and strain rate estimates.

4.5. Stress Versus Strength Relationship

The viscosity controls the strength of the different model units, such as the crust. The maximum magnitudes of the differential stress in the crust do not vary significantly for a strong lithospheric mantle and different crustal viscosities (Figure 6a). Conversely, the maximum magnitudes of the horizontal velocities and strain rates in the crust vary between one and two orders of magnitude, respectively. The minor variation of maximum crustal differential stresses, despite two orders of magnitude variation in crustal viscosities, shows that crustal stress magnitudes are not a good proxy for the magnitude of crustal viscosity (e.g., Schmalholz et al., 2009). The reason is that the magnitude of the stress is controlled by the magnitude of ΔGPE, which is independent of viscosity, and the thickness of the crust. Smaller crustal viscosities result in faster horizontal velocities and higher strain rates. Therefore, stress magnitudes, which are proportional to the product of viscosity and strain rate, remain more or less constant for decreasing crustal viscosities.

4.6. Impact of Curvature

Our results show that the impact of the Earth's curvature on the stress field around continental plateaus is minor. The absolute magnitudes of stresses are slightly smaller in models considering the Earth's curvature compared to

flat models (Figure 13). If the curvature becomes larger, then differences between stresses for a rectangular and spherical geometry increase. However, the differences are not large (Figure 13). The minor impact of curvature for our model configuration is predicted by the simple geometrical shallow sheet scaling analysis of Section 2.1.

The consideration of curvature could have an impact on the calculation of frictional-plastic yielding in the uppermost few kilometers of the crust. The maximum differences in stress between models with and without curvature are between 5 and 10 MPa in the uppermost crust (Figure 13). Hence, the curvature can affect the position of the brittle-ductile transition. For studies focusing on stress magnitudes in the uppermost crust, such differences could be of interest.

The curvature of the lithosphere is more important for other scenarios compared to the plateau without far-field deformation studied here. For example, several numerical studies investigated the impact of a locally curved and geometrically stiffened plate on the India-Asia collision and related exhumation (e.g., Bendick & Ehlers, 2014; Koptev et al., 2019). Amongst others, these studies show that the geometrical stiffening effect might be important for localized regions with fast exhumation such as syntaxes. Furthermore, several theoretical studies investigated the impact of a spherical geometry on free subduction. Chamolly and Ribe (2021) found that the Earth's sphericity has a modest impact on the sinking speed of a slab but a much larger impact on the stress field in the slab which is important for the along-strike buckling of slabs. F. Chen et al. (2022) compared results of free subduction simulations in 3D Cartesian and spherical shell domains. They found differences between the simulations that are related, for example, to the reduction of space with depth in spherical shells which enhances along-strike buckling and trench curvature.

4.7. Simplifications

We make several simplifications in our model to study first-order features of the 3D stress field around continental plateaus and to keep the results transparent. We consider a simple and idealized geometry of a continental plateau and only the instantaneous stress field. We consider a rectangular corner geometry only while in nature many different corner geometries can exist with angles different from the 90-degree angle used here. We do not apply a far-field velocity field in order to isolate the impact of topography and lateral crustal thickness variation on the stress field. For the Tibetan plateau, the indentation of the Indian plate affects the deformation field.

Another limitation of our model is the simplified density and viscosity structure. 2D numerical models that consider a more realistic yield strength envelope exhibit significant vertical viscosity variations due to the temperature dependence of viscosity. These viscosity variations cause stronger vertical stress variations compared to our model because high stresses are focused in the high-viscosity levels of the crust and lithospheric mantle (e.g., Schmalholz et al., 2019). Also, several studies have proposed the existence of a low-viscosity middle or lower crustal layer in which significant crustal flow could take place (e.g., Beaumont et al., 2004; Clark & Royden, 2000). The existence of such a widespread and continuous low-viscosity crustal layer remains disputed (e.g., Nábělek et al., 2009). If such a low-viscosity layer existed, then the magnitudes of crustal differential stresses would likely be larger as predicted by our model because the vertically integrated stresses supporting the plateau would be focused on a thinner upper crustal, high-viscosity layer. Therefore, more realistic vertical viscosity variations result in larger maximum differential stresses compared to our model with constant viscosity in the model units.

Furthermore, the temperature dependence of viscosity will result in lateral variations of crustal and lithospheric mantle viscosites along the Moho between plateau and lowland because of different temperatures at different depths (e.g., Schmalholz et al., 2019). However, these lateral viscosity variations might not be dramatic in the lithospheric mantle because the potentially active low-temperature plasticity is significantly less sensitive to temperature than dislocation creep (e.g., England & Molnar, 2015).

4.8. Dimensionless Stress Ratio and Analytical Estimate for Horizontal Velocity

To derive the analytical estimate V_e, we assume that the estimated deviatoric stress in the crust, τ_e, causes horizontal extension of the plateau. In other words, by applying Equation 7 we assume that the gravitational stress is equal to the viscous flow stress and, hence, we assume

$$\frac{\rho_c g h_a L}{8 \eta_c V_e} \approx 1. \tag{14}$$

The above dimensionless stress ratio is similar to the Ramberg (Ramberg, 1981; Weijermars & Schmeling, 1986) and Argand numbers (England & McKenzie, 1982). The Ramberg and Argand numbers scale the gravitational stress to a viscous stress. In the Ramberg number, the strain rate is usually expressed by the ratio of a velocity to a length scale (e.g., Medvedev, 2002). Conversely, in the Argand number the strain rate is typically assumed to be the large-scale lithospheric shortening rate during crustal thickening (England & McKenzie, 1982) or crustal and lithospheric folding (Schmalholz et al., 2002).

To quantify the Ramberg number, one commonly assumes $L = h_a$ (Ramberg, 1981; Weijermars & Schmeling, 1986). Medvedev (2002) applied the Ramberg number to a two-sided wedge of total width λ with a basal shear velocity V_{bs}. They estimated the strain rate with the ratio V_{bs}/λ. In our model, a cross-section orthogonal across the transition zone with a linear change of topography corresponds to a geometry similar to one-half of the double-sided wedge considered by Medvedev (2002). In our analytical velocity estimate, we used a length scale of $L = 200$ km which is equivalent to twice the width of the transition zone. This length scale is similar to the one used in the analytical model for two-sided wedges by Medvedev (2002) to estimate strain rates. Hence, we expect that our velocity estimate is also applicable to plateau geometries with transition widths different from the ones of our model if in the analytical estimate twice the width of the transition zone is used as length scale L.

4.9. Applications to the Tibetan Plateau

The Tibetan plateau has been the focus of many theoretical studies on lithospheric stress and viscosities (e.g., England & Houseman, 1988; England & Molnar, 1997; Flesch et al., 2001; Ghosh et al., 2006; Jeffreys, 1932; Liu & Yang, 2003; Molnar & Lyon-Caen, 1988; Molnar et al., 1993; Warners-Ruckstuhl et al., 2013). Here, we use our model result that indicates that the Ramberg number is ≈ 1 (Equation 14) to estimate the crustal viscosity in particular regions of the Tibetan plateau. For example, in the eastern Tibetan plateau the Longmen Shan orogenic belt represents the boundary between the Tibetan plateau and the Sichuan Basin (e.g., Sun et al., 2019). In the southern segment of the Longmen Shan, the altitude decreases ≈ 4 km over a distance of ≈ 50 km and in the northern segment the altitude decreases ≈ 3.5 km over a distance of ≈ 200 km (e.g., Sun et al., 2019). The crustal thickness around the Longmen Shan with ≈ 4 km topography is ≈ 60 km indicating a situation close to isostatic equilibrium (Z. Zhang et al., 2009). The GPS velocities indicate a horizontal velocity in the direction from the high to the low topographic region of ≈ 1 cm/year (e.g., Gan et al., 2007; Penney & Copley, 2021; Zheng et al., 2017). We solve Equation 14 for the crustal viscosity which yields

$$\eta_c \approx \frac{\rho_c g h_a L}{8 V_e}. \tag{15}$$

Applying $V_e = 1$ cm/year, $\rho_c = 2{,}800$ kg/m³, $h_a = 4$ km and $L = 100$ km provides an estimate for the average crustal viscosity of $\approx 5 \cdot 10^{21}$ Pa · s. Changing h_a to 3.5 km and L to 400 km provides $\eta_c \approx 1.5 \cdot 10^{22}$ Pa · s. Given the uncertainties of the measured quantities such as velocities and topography as well as of the simple mathematical model, our model predicts effective average crustal viscosities of $\approx 10^{22}$ Pa · s. This viscosity value estimated with our simple Equation 15 agrees with viscosity estimates of other studies that applied more elaborated thin viscous sheet models (e.g., England & Molnar, 1997; Flesch et al., 2001).

The analysis of GPS measurements across the Tibetan plateau indicates that the deformation of a continuous medium, such as modeled in our study, best describes the present-day tectonics of the Tibetan Plateau; at least when averaged over distances of $> \approx 100$ km (e.g., Ge et al., 2015; P.-Z. Zhang et al., 2004). Ge et al. (2015) analyzed GPS measurements and concluded that the Tibetan plateau is undergoing similar dilatation in its northern, southern and southwestern parts. Dilatation occurs by vertical thinning, with strain rates of $\approx 8 \cdot 10^{-9}$ 1/year, approximately N-S shortening, with strain rates of $\approx 12 \cdot 10^{-9}$ 1/year and approximately E-W extension, with strain rates of $\approx 20 \cdot 10^{-9}$ 1/year. These average extensional strain rates are representative for the Tibetan plateau and are only slightly smaller than the smallest of the maximum strain rates in our models, having values of $\approx 80 \cdot 10^{-9}$ 1/year (Figure 15b). The smallest maximum strain rates in our models correspond to the smallest extensional velocities (Figure 15b) and, hence, to the largest crustal viscosity of 10^{22} Pa · s (Figure 5). The first-

order comparison between measured and modeled extensional strain rates also suggests that 10^{22} Pa · s is a reasonable average viscosity for the Tibetan crust.

The India-Asia collision and the formation of the Tibetan plateau have generated a variety of large-scale strike-slip faults, particularly around the two syntaxes regions (e.g., Harrison et al., 1992; Molnar & Tapponnier, 1975; Royden et al., 1997; Tapponnier et al., 2001). The syntaxes regions are characterized by significant horizontal changes in the direction of the transition zone between high- and low-altitude regions. In our model, the corner represents such regions in which the transition zone between high- and low-altitude regions significantly changes its horizontal direction. The modeled, strongly increased, horizontal shear stresses around the plateau's corner region (Figures 7 and 8) suggest that ongoing strike-slip faulting around the Tibetan syntaxes regions might be supported, in addition to indentation and convergence, by horizontal shear stresses resulting from the significant lateral changes in topography and crustal thickness.

A stronger continental crust exhibits larger and more homogeneously distributed differential stresses compared to a weaker crust above a strong lithospheric mantle (Figures 9a and 9c). For a weak, low-viscosity crust, large differential stresses occur only along the transition zone and differential stresses significantly decrease toward the plateau center (Figure 9c). Earthquakes are relatively equally distributed across the Tibetan plateau (e.g., Bai et al., 2017; Hetényi et al., 2023; Li & Hou, 2019). There is no systematic trend that shows, for example, a decreasing density of earthquakes toward the center of the Tibetan plateau. Consequently, the crust of the Tibetan plateau should be at least strong enough to prohibit a considerable decrease of differential stress toward the plateau center.

Some of the most active orogenic processes on Earth occur within the syntaxes of the Himalayan chain, at the southern termination of the Tibetan plateau (e.g., Zeitler et al., 2001). These syntaxial regions are characterized by strong lateral variations in topography and crustal thickness. The applied power-law viscous flow law can locally decrease crustal viscosities in regions with stresses that are larger than those in the surroundings, due to its stress-weakening effect. Our results show that such relative stress weakening can occur in the transition zone around the corner region (Figure 10f). The decreased viscosity in the transition at the corner of the plateau could locally weaken the crust, focus the deformation and contribute to locally increased exhumation. Several mechanisms have been proposed to explain the localized exhumation and deformation in the syntaxes, such as crustal-scale buckle folding (Burg et al., 1997), diverted crustal flow resulting from localized river incision and erosion (Zeitler et al., 2001) or crustal deformation over a geometrically stiffened subducting plate (Bendick & Ehlers, 2014). Whatever the mechanism, a local stress-weakening of the crust in the syntaxes region due to stresses resulting from strong lateral topography and crustal thickness variations could support the localization of deformation and ongoing rapid exhumation.

5. Conclusions

We investigated with 3D numerical calculations the interplay of various factors governing the crustal stresses and horizontal velocities caused by continental plateaus. In our model, the plateau deforms by horizontal dilatation and vertical thinning due to lateral variations in GPE only because we do not consider any tectonic far-field deformation.

Varying the viscosity of both the continental crust and lithospheric mantle has unveiled several key insights (Sections 3.3 and 3.5). First, maximum horizontal velocities in the crust always increase with decreasing viscosity of the crust and lithospheric mantle. Second, decreasing crustal and lithospheric mantle viscosities does not automatically reduce the maximum stress magnitudes in the crust; instead, the decrease can lead to faster crustal flow, higher strain rates, and subsequently, higher stresses. Maximum crustal stress magnitudes vary within a factor of 2 only while crustal and lithospheric mantle viscosities vary by two orders of magnitude. Hence, in deforming regions crustal stress magnitudes are not a reliable proxy for the effective crustal viscosity, and, hence, crustal strength. Lastly, the incorporation of a stress-dependent power-law viscous flow law generally results in decreased stress magnitudes.

We performed a scaling analysis and derived simple analytical estimates for the crustal horizontal deviatoric stress and horizontal velocities caused by continental plateaus. The analytical estimates agree to first order with the 3D numerical results (Section 3.7). We applied the scaling results to estimate average crustal viscosities for the eastern Tibetan plateau and obtained a crustal viscosity of $\approx 10^{22}$ Pa · s which is in agreement with estimates of

other studies (Section 4.9). This crustal viscosity magnitude also agrees with the results of our systematic numerical calculations (Section 3.3). We defined a critical velocity threshold for assessing the continental crust's effective viscosity. For instance, modeled Tibetan plateau horizontal velocities exceeding 4 cm/year suggest an unrealistically weak continental crust. In all scenarios explored, an average crustal viscosity of at least $3 \cdot 10^{21}$ Pa $\cdot$ s is essential to ensure velocities below 4 cm/year. The maximum differential stresses in the crust are between 55 and 115 MPa for all scenarios. This underscores the importance of a mechanically strong crust to sustain large topographic features and lateral crustal thickness variations over extended geological time scales.

Our study has emphasized the critical role played by plateau corner regions in shaping the crustal stress field (Section 3.4). Notably, horizontal deviatoric normal stresses consistently decrease toward the rectangular corner considered here, while horizontal shear stresses significantly intensify. These corner regions exhibit elevated horizontal shear stresses, reaching up to 30 MPa in our models, underscoring their importance in understanding crustal stress patterns.

Finally, we have demonstrated with a simple shallow sheet scaling in combination with 3D numerical calculations considering spherical geometries that for our model the Earth's curvature exerts a minor influence on stress magnitudes and distribution within the continental crust (Section 3.6). Consequently, for spatial scales smaller than a few thousand kilometers, it is justifiable to omit the Earth's curvature in numerical models of stress distribution around continental plateaus.

Appendix A: Method

A1. Mathematical Model

In this study, we use a numerical algorithm to solve the Stokes equations in spherical coordinates. In this coordinates system, r is the radial direction, θ is the polar angle and φ is the azimuthal angle (see Figure 2b). The total stress tensor σ_{ij} is decomposed into a pressure P (or mean stress) and a deviatoric stress τ_{ij} as $\sigma_{ij} = -\delta_{ij}P + \tau_{ij}$. The indexes i and j vary between 1 and 3 and indicate the three spatial directions (r, θ, φ). Components of the deviatoric stress tensor for incompressible flow are defined as:

$$
\begin{aligned}
\tau_{rr} &= 2\eta_{\mathrm{E}}\dot{\epsilon}_{rr} = 2\eta_{\mathrm{E}}\left(\frac{\partial V_r}{\partial r}\right) \\
\tau_{\theta\theta} &= 2\eta_{\mathrm{E}}\dot{\epsilon}_{\theta\theta} = 2\eta_{\mathrm{E}}\left(\frac{1}{r}\frac{\partial V_\theta}{\partial\theta} + \frac{V_r}{r}\right) \\
\tau_{\varphi\varphi} &= 2\eta_{\mathrm{E}}\dot{\epsilon}_{\varphi\varphi} = 2\eta_{\mathrm{E}}\left(\frac{1}{r\sin(\theta)}\frac{\partial V_\varphi}{\partial\varphi} + \frac{V_r}{r} + \frac{V_\theta}{r}\cot(\theta)\right) \\
\tau_{r\theta} &= 2\eta_{\mathrm{E}}\dot{\epsilon}_{r\theta} = 2\eta_{\mathrm{E}}\left(\frac{1}{2}\left(\frac{\partial V_\theta}{\partial r} + \frac{1}{r}\frac{\partial V_r}{\partial\theta} - \frac{V_\theta}{r}\right)\right) \\
\tau_{r\varphi} &= 2\eta_{\mathrm{E}}\dot{\epsilon}_{r\varphi} = 2\eta_{\mathrm{E}}\left(\frac{1}{2}\left(\frac{\partial V_\varphi}{\partial r} + \frac{1}{r\sin(\theta)}\frac{\partial V_r}{\partial\varphi} - \frac{V_\varphi}{r}\right)\right) \\
\tau_{\theta\varphi} &= 2\eta_{\mathrm{E}}\dot{\epsilon}_{\theta\varphi} = 2\eta_{\mathrm{E}}\left(\frac{1}{2}\left(\frac{1}{r}\frac{\partial V_\varphi}{\partial\theta} + \frac{1}{r\sin(\theta)}\frac{\partial V_\theta}{\partial\varphi} - \frac{V_\varphi}{r}\cot(\theta)\right)\right)
\end{aligned}
\tag{A1}
$$

where η_E is the effective viscosity, $\dot{\epsilon}_{ij}$ are the strain rate tensor components and V_i are the components of the velocity vector. The square root of the second invariant of the deviatoric stress tensor, τ_{II}, which is used in Equation 11 for the stress-dependent viscosity, is

$$
\tau_{\mathrm{II}} = \sqrt{0.5\,\tau_{ij}^2} = \sqrt{0.5(\tau_{\mathrm{rr}}^2 + \tau_{\theta\theta}^2 + \tau_{\varphi\varphi}^2) + \tau_{\mathrm{r}\theta}^2 + \tau_{\mathrm{r}\varphi}^2 + \tau_{\theta\varphi}^2}.
\tag{A2}
$$

The equations for the conservation of mass and the conservation of the linear momentum in an incompressible fluid under gravity are:

$$0 = -\left(\frac{\partial V_r}{\partial r} + \frac{1}{r}\frac{\partial V_\theta}{\partial \theta} + \frac{1}{r\sin(\theta)}\frac{\partial V_\varphi}{\partial \varphi} + 2\frac{V_r}{r} + \frac{V_\theta}{r}\cot(\theta) \right)$$

$$0 = \frac{\partial \sigma_{rr}}{\partial r} + \frac{1}{r}\frac{\partial \tau_{r\theta}}{\partial \theta} + \frac{1}{r\sin(\theta)}\frac{\partial \tau_{r\varphi}}{\partial \varphi} + 2\frac{\sigma_{rr}}{r} - \frac{\sigma_{\theta\theta}}{r} - \frac{\sigma_{\varphi\varphi}}{r} + \frac{\tau_{r\theta}}{r}\cot(\theta) - \rho g$$

$$0 = \frac{\partial \tau_{r\theta}}{\partial r} + \frac{1}{r}\frac{\partial \sigma_{\theta\theta}}{\partial \theta} + \frac{1}{r\sin(\theta)}\frac{\partial \tau_{\theta\varphi}}{\partial \varphi} + 3\frac{\tau_{r\theta}}{r} + \frac{\sigma_{\theta\theta}}{r}\cot(\theta) - \frac{\sigma_{\varphi\varphi}}{r}\cot(\theta)$$

$$0 = \frac{\partial \tau_{r\varphi}}{\partial r} + \frac{1}{r}\frac{\partial \tau_{\theta\varphi}}{\partial \theta} + \frac{1}{r\sin(\theta)}\frac{\partial \sigma_{\varphi\varphi}}{\partial \varphi} + 3\frac{\tau_{r\varphi}}{r} + 2\frac{\tau_{\theta\varphi}}{r}\cot(\theta)$$

(A3)

where ρ is the density and g is the gravitational acceleration.

A2. Numerical Method

The numerical algorithm to solve the governing system of equations is programmed for spherical coordinates. To solve the governing equations, we discretize them on a staggered grid with constant spacing using the finite difference method (e.g., Gerya, 2019; Räss et al., 2022; Virieux, 1986). The numerical method we use to solve the discretized equations is the pseudo-transient method, which is an iterative solution strategy for stationary problems that allows solving the equations in a matrix-free way (e.g., Räss et al., 2022; Wang et al., 2022). The pseudo-transient method consists of adding a pseudo-time derivative to the governing equations. The initial values for the pressure and velocity fields do not solve the discretized equations. Hence, the idea of the pseudo-transient method is to iterate over the pseudo-time until the pseudo-time derivatives become smaller than a specified tolerance value for all numerical grid points, and a numerical solution is reached.

The pseudo-transient method consists in adding a pseudo-time derivative to Equations A1 and A3:

$$\frac{1}{2\tilde{G}}\frac{\partial \tau_{rr}}{\partial \tau_{PT}} + \frac{\tau_{rr}}{2\eta_E} = \frac{\partial V_r}{\partial r}$$

$$\frac{1}{2\tilde{G}}\frac{\partial \tau_{\theta\theta}}{\partial \tau_{PT}} + \frac{\tau_{\theta\theta}}{2\eta_E} = \frac{1}{r}\frac{\partial V_\theta}{\partial \theta} + \frac{V_r}{r}$$

$$\frac{1}{2\tilde{G}}\frac{\partial \tau_{\varphi\varphi}}{\partial \tau_{PT}} + \frac{\tau_{\varphi\varphi}}{2\eta_E} = \frac{1}{r\sin(\theta)}\frac{\partial V_\varphi}{\partial \varphi} + \frac{V_r}{r} + \frac{V_\theta}{r}\cot(\theta)$$

$$\frac{1}{2\tilde{G}}\frac{\partial \tau_{r\theta}}{\partial \tau_{PT}} + \frac{\tau_{r\theta}}{2\eta_E} = \frac{1}{2}\left(\frac{\partial V_\theta}{\partial r} + \frac{1}{r}\frac{\partial V_r}{\partial \theta} - \frac{V_\theta}{r} \right)$$

$$\frac{1}{2\tilde{G}}\frac{\partial \tau_{r\varphi}}{\partial \tau_{PT}} + \frac{\tau_{r\varphi}}{2\eta_E} = \frac{1}{2}\left(\frac{\partial V_\varphi}{\partial r} + \frac{1}{r\sin(\theta)}\frac{\partial V_r}{\partial \varphi} - \frac{V_\varphi}{r} \right)$$

$$\frac{1}{2\tilde{G}}\frac{\partial \tau_{\theta\varphi}}{\partial \tau_{PT}} + \frac{\tau_{\theta\varphi}}{2\eta_E} = \frac{1}{2}\left(\frac{1}{r}\frac{\partial V_\varphi}{\partial \theta} + \frac{1}{r\sin(\theta)}\frac{\partial V_\theta}{\partial \varphi} - \frac{V_\varphi}{r}\cot(\theta) \right)$$

$$\frac{1}{\tilde{K}}\frac{\partial P}{\partial \tau_{PT}} = -\left(\frac{\partial V_r}{\partial r} + \frac{1}{r}\frac{\partial V_\theta}{\partial \theta} + \frac{1}{r\sin(\theta)}\frac{\partial V_\varphi}{\partial \varphi} + 2\frac{V_r}{r} - \frac{V_\theta}{r}\cot(\theta) \right)$$

$$\tilde{\rho}\frac{\partial V_r}{\partial \tau_{PT}} = \frac{\partial \sigma_{rr}}{\partial r} + \frac{1}{r}\frac{\partial \tau_{r\theta}}{\partial \theta} + \frac{1}{r\sin(\theta)}\frac{\partial \tau_{r\varphi}}{\partial \varphi} + 2\frac{\sigma_{rr}}{r} - \frac{\sigma_{\theta\theta}}{r} - \frac{\sigma_{\varphi\varphi}}{r} + \frac{\tau_{r\theta}}{r}\cot(\theta) - \rho g$$

$$\tilde{\rho}\frac{\partial V_\theta}{\partial \tau_{PT}} = \frac{\partial \tau_{r\theta}}{\partial r} + \frac{1}{r}\frac{\partial \sigma_{\theta\theta}}{\partial \theta} + \frac{1}{r\sin(\theta)}\frac{\partial \tau_{\theta\varphi}}{\partial \varphi} + 3\frac{\tau_{r\theta}}{r} + \frac{\sigma_{\theta\theta}}{r}\cot(\theta) - \frac{\sigma_{\varphi\varphi}}{r}\cot(\theta)$$

$$\tilde{\rho}\frac{\partial V_\varphi}{\partial \tau_{PT}} = \frac{\partial \tau_{r\varphi}}{\partial r} + \frac{1}{r}\frac{\partial \tau_{\theta\varphi}}{\partial \theta} + \frac{1}{r\sin(\theta)}\frac{\partial \sigma_{\varphi\varphi}}{\partial \varphi} + 3\frac{\tau_{r\varphi}}{r} + 2\frac{\tau_{\theta\varphi}}{r}\cot(\theta)$$

(A4)

where $\tilde{K}$, $\tilde{\rho}$ and $\tilde{G}$ are numerical parameters and τ_{PT} is a pseudo-time. $\tilde{K}$ and $\tilde{G}$ can be considered as pseudo-bulk and pseudo-shear modulus, respectively, and $\tilde{\rho}$ as a pseudo-density. With these parameters, Equation A4 can be considered as acoustic and inertial approximations of the mass and momentum balance equations respectively. After a number of iterations, the pseudo-time derivatives become smaller than a specified tolerance, here $5 \cdot 10^{-7}$, and a numerical solution is reached.

Data Availability Statement

Current and future versions of the SphericalStokes.jl software used in this study are publicly available on GitHub at https://github.com/PTsolvers/SphericalStokes. The exact version used in this study is archived on Zenodo and can be accessed at https://zenodo.org/doi/10.5281/zenodo.10093648 (Macherel, Räss, & Schmalholz, 2023).

References

Allmann, B. P., & Shearer, P. M. (2009). Global variations of stress drop for moderate to large earthquakes. *Journal of Geophysical Research*, *114*(B1). https://doi.org/10.1029/2008jb005821

Artyushkov, E. (1973). Stresses in the lithosphere caused by crustal thickness inhomogeneities. *Journal of Geophysical Research*, *78*(32), 7675–7708. https://doi.org/10.1029/jb078i032p07675

Bai, L., Li, G., Khan, N. G., Zhao, J., & Ding, L. (2017). Focal depths and mechanisms of shallow earthquakes in the Himalayan–Tibetan region. *Gondwana Research*, *41*, 390–399. https://doi.org/10.1016/j.gr.2015.07.009

Beaumont, C., Jamieson, R. A., Nguyen, M. H., & Medvedev, S. (2004). Crustal channel flows: 1. Numerical models with applications to the tectonics of the Himalayan-Tibetan orogen. *Journal of Geophysical Research*, *109*(B6), B06406. https://doi.org/10.1029/2003jb002809

Bendick, R., & Ehlers, T. A. (2014). Extreme localized exhumation at syntaxes initiated by subduction geometry. *Geophysical Research Letters*, *41*(16), 5861–5867. https://doi.org/10.1002/2014gl061026

Bird, P., & Piper, K. (1980). Plane-stress finite-element models of tectonic flow in southern California. *Physics of the Earth and Planetary Interiors*, *21*(2–3), 158–175. https://doi.org/10.1016/0031-9201(80)90067-9

Bischoff, S., & Flesch, L. (2019). Impact of lithospheric strength distribution on India-Eurasia deformation from 3-D geodynamic models. *Journal of Geophysical Research: Solid Earth*, *124*(1), 1084–1105. https://doi.org/10.1029/2018jb015704

Bott, M., & Kusznir, N. (1984). The origin of tectonic stress in the lithosphere. *Tectonophysics*, *105*(1–4), 1–13. https://doi.org/10.1016/0040-1951(84)90190-2

Bronstein, I., Semendyayev, K., Musiol, G., & Mühlig, H. (2015). *Handbook of mathematics*. Springer Berlin.

Burg, J.-P., Davy, P., Nievergelt, P., Oberli, F., Seward, D., Diao, Z., & Meier, M. (1997). Exhumation during crustal folding in the Namche-Barwa syntaxis. *Terra Nova*, *9*(2), 53–56. https://doi.org/10.1111/j.1365-3121.1997.tb00001.x

Chamolly, A., & Ribe, N. M. (2021). Fluid mechanics of free subduction on a sphere. Part 1. The axisymmetric case. *Journal of Fluid Mechanics*, *929*, A22. https://doi.org/10.1017/jfm.2021.871

Chen, F., Davies, D. R., Goes, S., Suchoy, L., & Kramer, S. C. (2022). Comparing the dynamics of free subduction in Cartesian and spherical domains. *Geochemistry, Geophysics, Geosystems*, *23*(12), e2022GC010757. https://doi.org/10.1029/2022gc010757

Chen, L., Liu, L., Capitanio, F. A., Gerya, T. V., & Li, Y. (2020). The role of pre-existing weak zones in the formation of the Himalaya and Tibetan plateau: 3-D thermomechanical modelling. *Geophysical Journal International*, *221*(3), 1971–1983. https://doi.org/10.1093/gji/ggaa125

Clark, M. K., & Royden, L. H. (2000). Topographic ooze: Building the eastern margin of Tibet by lower crustal flow. *Geology*, *28*(8), 703–706. https://doi.org/10.1130/0091-7613(2000)028<0703:tobtem>2.3.co;2

Coblentz, D. D., Richardson, R. M., & Sandiford, M. (1994). On the gravitational potential of the Earth's lithosphere. *Tectonics*, *13*(4), 929–945. https://doi.org/10.1029/94tc01033

Copley, A., & McKenzie, D. (2007). Models of crustal flow in the India-Asia collision zone. *Geophysical Journal International*, *169*(2), 683–698. https://doi.org/10.1111/j.1365-246x.2007.03343.x

Crameri, F., Schmeling, H., Golabek, G., Duretz, T., Orendt, R., Buiter, S., et al. (2012). A comparison of numerical surface topography calculations in geodynamic modelling: An evaluation of the 'sticky air' method. *Geophysical Journal International*, *189*(1), 38–54. https://doi.org/10.1111/j.1365-246x.2012.05388.x

D'Agostino, N., England, P., Hunstad, I., & Selvaggi, G. (2014). Gravitational potential energy and active deformation in the Apennines. *Earth and Planetary Science Letters*, *397*, 121–132. https://doi.org/10.1016/j.epsl.2014.04.013

Dalmayrac, B., & Molnar, P. (1981). Parallel thrust and normal faulting in Peru and constraints on the state of stress. *Earth and Planetary Science Letters*, *55*(3), 473–481. https://doi.org/10.1016/0012-821x(81)90174-6

Darwin, G. (1882). On the stresses caused in the interior of the Earth by the weight of continents and mountains. *Philosophical Transactions of the Royal Society*, *173*, 187–230.

Doin, M.-P., Twardzik, C., Ducret, G., Lasserre, C., Guillaso, S., & Jianbao, S. (2015). InSAR measurement of the deformation around Siling Co Lake: Inferences on the lower crust viscosity in central Tibet. *Journal of Geophysical Research: Solid Earth*, *120*(7), 5290–5310. https://doi.org/10.1002/2014jb011768

Dziewonski, A. M., & Anderson, D. L. (1981). Preliminary reference Earth model. *Physics of the Earth and Planetary Interiors*, *25*(4), 297–356. https://doi.org/10.1016/0031-9201(81)90046-7

Engelder, T. (2014). *Stress regimes in the lithosphere* (Vol. 151). Princeton University Press.

England, P., & Houseman, G. (1988). The mechanics of the Tibetan plateau. *Philosophical Transactions of the Royal Society of London. Series A, Mathematical and Physical Sciences*, *326*(1589), 301–320.

England, P., Houseman, G., & Nocquet, J.-M. (2016). Constraints from GPS measurements on the dynamics of deformation in Anatolia and the Aegean. *Journal of Geophysical Research: Solid Earth*, *121*(12), 8888–8916. https://doi.org/10.1002/2016jb013382

England, P., & McKenzie, D. (1982). A thin viscous sheet model for continental deformation. *Geophysical Journal International*, *70*(2), 295–321. https://doi.org/10.1111/j.1365-246x.1982.tb04969.x

England, P., & Molnar, P. (1997). Active deformation of Asia: From kinematics to dynamics. *Science*, *278*(5338), 647–650. https://doi.org/10.1126/science.278.5338.647

England, P., & Molnar, P. (2015). Rheology of the lithosphere beneath the central and western Tien Shan. *Journal of Geophysical Research: Solid Earth*, *120*(5), 3803–3823. https://doi.org/10.1002/2014jb011733

England, P., Walker, R. T., Fu, B., & Floyd, M. A. (2013). A bound on the viscosity of the Tibetan crust from the horizontality of palaeolake shorelines. *Earth and Planetary Science Letters*, *375*, 44–56. https://doi.org/10.1016/j.epsl.2013.05.001

Fleitout, L., & Froidevaux, C. (1982). Tectonics and topography for a lithosphere containing density heterogeneities. *Tectonics*, *1*(1), 21–56. https://doi.org/10.1029/tc001i001p00021

Flesch, L. M., Haines, A. J., & Holt, W. E. (2001). Dynamics of the India-Eurasia collision zone. *Journal of Geophysical Research*, *106*(B8), 16435–16460. https://doi.org/10.1029/2001jb000208

Frank, F. (1972). Plate tectonics, the analogy with glacier flow, and isostasy. In *Washington DC American Geophysical Union Geophysical Monograph Series* (Vol. *16*, pp. 285–292).

Gan, W., Zhang, P., Shen, Z.-K., Niu, Z., Wang, M., Wan, Y., et al. (2007). Present-day crustal motion within the Tibetan plateau inferred from GPS measurements. *Journal of Geophysical Research*, *112*(B8). https://doi.org/10.1029/2005JB004120doi:10.1029/2005JB004120

Ge, W.-P., Molnar, P., Shen, Z.-K., & Li, Q. (2015). Present-day crustal thinning in the southern and northern Tibetan plateau revealed by GPS measurements. *Geophysical Research Letters*, *42*(13), 5227–5235. https://doi.org/10.1002/2015gl064347

Gerya, T. (2019). Introduction to numerical geodynamic modelling.

Ghosh, A., Holt, W. E., & Flesch, L. M. (2009). Contribution of gravitational potential energy differences to the global stress field. *Geophysical Journal International*, *179*(2), 787–812. https://doi.org/10.1111/j.1365-246x.2009.04326.x

Ghosh, A., Holt, W. E., Flesch, L. M., & Haines, A. J. (2006). Gravitational potential energy of the Tibetan plateau and the forces driving the Indian plate. *Geology*, *34*(5), 321–324. https://doi.org/10.1130/g22071.1

Hardebeck, J. L., & Okada, T. (2018). Temporal stress changes caused by earthquakes: A review. *Journal of Geophysical Research: Solid Earth*, *123*(2), 1350–1365. https://doi.org/10.1002/2017jb014617

Harrison, T. M., Copeland, P., Kidd, W., & Yin, A. (1992). Raising Tibet. *Science*, *255*(5052), 1663–1670. https://doi.org/10.1126/science.255.5052.1663

Hetényi, G., Vergne, J., Bollinger, L., Subedi, S., Michailos, K., & Drukpa, D. (2023). Seismological imaging and current seismicity of the Himalayan arc. In *Himalaya, dynamics of a giant 1: Geodynamic setting of the Himalayan range* (pp. 101–128).

Hirschberg, H., Lamb, S., & Savage, M. (2019). Strength of an obliquely convergent plate boundary: Lithospheric stress magnitudes and viscosity in New Zealand. *Geophysical Journal International*, *216*(2), 1005–1024. https://doi.org/10.1093/gji/ggy477

Hirth, G., & Kohlstedt, D. (2003). Rheology of the upper mantle and the mantle wedge: A view from the experimentalists. *Geophysical Monograph-American Geophysical Union*, *138*, 83–106. https://doi.org/10.1029/138GM06

Houseman, G., & England, P. (1986). Finite strain calculations of continental deformation: 1. Method and general results for convergent zones. *Journal of Geophysical Research*, *91*(B3), 3651–3663. https://doi.org/10.1029/jb091ib03p03651

Jeffreys, H. (1932). On the stresses in the Earth's crust required to support surface inequalities. (second paper). *Geophysical Journal International*, *3*, 60–69. https://doi.org/10.1111/j.1365-246x.1932.tb00400.x

Kanamori, H. (1980). The state of stress in the Earth's lithosphere.

Karato, S.-I. (2008). Deformation of Earth materials. An introduction to the rheology of solid Earth (Vol. *463*). https://doi.org/10.1017/CBO9780511804892

Kind, R., Yuan, X., Saul, J., Nelson, D., Sobolev, S., Mechie, J., et al. (2002). Seismic images of crust and upper mantle beneath Tibet: Evidence for Eurasian plate subduction. *Science*, *298*(5596), 1219–1221. https://doi.org/10.1126/science.1078115

Kohlstedt, D., Evans, B., & Mackwell, S. (1995). Strength of the lithosphere: Constraints imposed by laboratory experiments. *Journal of Geophysical Research*, *100*(B9), 17587–17602. https://doi.org/10.1029/95jb01460

Koptev, A., Ehlers, T. A., Nettesheim, M., & Whipp, D. M. (2019). Response of a rheologically stratified lithosphere to subduction of an indenter-shaped plate: Insights into localized exhumation at orogen syntaxes. *Tectonics*, *38*(6), 1908–1930. https://doi.org/10.1029/2018tc005455

Lamb, S. (2000). Active deformation in the Bolivian Andes, South America. *Journal of Geophysical Research*, *105*(B11), 25627–25653. https://doi.org/10.1029/2000jb900187

Laske, G., Masters, G., Ma, Z., & Pasyanos, M. (2013). Update on crust1. 0—A 1-degree global model of Earth's crust. In *Geophysical research abstracts* (Vol. 15, p. 2658).

Lechmann, S. M., Schmalholz, S. M., Hetényi, G., May, D. A., & Kaus, B. J. P. (2014). Quantifying the impact of mechanical layering and underthrusting on the dynamics of the modern India-Asia collisional system with 3-D numerical models. *Journal of Geophysical Research: Solid Earth*, *119*(1), 616–644. https://doi.org/10.1002/2012jb009748

Li, J., & Hou, G. (2019). Stress development in heterogeneous lithosphere: Insights into earthquake initiation in the Tan-Lu fault zone. *Tectonophysics*, *750*, 329–343. https://doi.org/10.1016/j.tecto.2018.11.018

Liang, S., Gan, W., Shen, C., Xiao, G., Liu, J., Chen, W., et al. (2013). Three-dimensional velocity field of present-day crustal motion of the Tibetan plateau derived from GPS measurements. *Journal of Geophysical Research: Solid Earth*, *118*(10), 5722–5732. https://doi.org/10.1002/2013jb010503

Lithgow-Bertelloni, C., & Guynn, J. H. (2004). Origin of the lithospheric stress field. *Journal of Geophysical Research*, *109*(B1). https://doi.org/10.1029/2003jb002467

Liu, M., & Yang, Y. (2003). Extensional collapse of the Tibetan plateau: Results of three-dimensional finite element modeling. *Journal of Geophysical Research*, *108*(B8), B082361. https://doi.org/10.1029/2002jb002248

Macherel, E., Podladchikov, Y., Ludovic, R., & Schmalholz, S. (2023). Quantifying diapir ascent velocities in power-law viscous rock under far-field stress: Integrating analytical estimates, 3D numerical calculations and geodynamic applications. *Geochemistry, Geophysics, Geosystems*, *24*(12), e2023GC011115. https://doi.org/10.1029/2023gc011115

Macherel, E., Räss, L., & Schmalholz, S. M. (2023). PTsolvers/SphericalStokes: SphericalStokes.jl 1.0.1 [Software]. *Zenodo*. https://doi.org/10.5281/zenodo.10093728

Malvern, L. E. (1969). *Introduction to the mechanics of a continuous medium*. Prentice-Hall, Inc.

McGarr, A., & Gay, N. (1978). State of stress in the Earth's crust. *Annual Review of Earth and Planetary Sciences*, *6*(1), 405–436. https://doi.org/10.1146/annurev.ea.06.050178.002201

Medvedev, S. (2002). Mechanics of viscous wedges: Modeling by analytical and numerical approaches. *Journal of Geophysical Research*, *107*(B6), ETG9-1–ETG9-15. https://doi.org/10.1029/2001JB000145

Medvedev, S., & Podladchikov, Y. Y. (1999). New extended thin-sheet approximation for geodynamic applications—I. Model formulation. *Geophysical Journal International*, *136*(3), 567–585. https://doi.org/10.1046/j.1365-246x.1999.00734.x

Mei, S., Suzuki, A., Kohlstedt, D., Dixon, N., & Durham, W. (2010). Experimental constraints on the strength of the lithospheric mantle. *Journal of Geophysical Research*, *115*(B8). https://doi.org/10.1029/2009jb006873

Molnar, P., England, P., & Martinod, J. (1993). Mantle dynamics, uplift of the Tibetan plateau, and the Indian monsoon. *Reviews of Geophysics*, *31*(4), 357–396. https://doi.org/10.1029/93rg02030

Molnar, P., & Lyon-Caen, H. (1988). Some simple physical aspects of the support, structure, and evolution of mountain belts. In *Processes in continental lithospheric deformation* (Vol. 218, pp. 179–207).

Molnar, P., & Tapponnier, P. (1975). Cenozoic tectonics of Asia: Effects of a continental collision: Features of recent continental tectonics in Asia can be interpreted as results of the India-Eurasia collision. *Science*, *189*(4201), 419–426. https://doi.org/10.1126/science.189.4201.419

Nábělek, J., Hetényi, G., Vergne, J., Sapkota, S., Kafle, B., Jiang, M., et al. (2009). Underplating in the Himalaya-Tibet collision zone revealed by the Hi-CLIMB experiment. *Science*, *325*(5946), 1371–1374. https://doi.org/10.1126/science.1167719

Parsons, B., & Richter, F. M. (1980). A relation between the driving force and geoid anomaly associated with mid-ocean ridges. *Earth and Planetary Science Letters*, *51*(2), 445–450. https://doi.org/10.1016/0012-821x(80)90223-x

Penney, C., & Copley, A. (2021). Lateral variations in lower crustal strength control the temporal evolution of mountain ranges: Examples from south-east Tibet. *Geochemistry, Geophysics, Geosystems*, *22*(2), e2020GC009092. https://doi.org/10.1029/2020gc009092

Philpotts, A. R., & Ague, J. J. (2022). *Principles of igneous and metamorphic petrology*. Cambridge University Press.

Pini, V., Ruz, J. J., Kosaka, P. M., Malvar, O., Calleja, M., & Tamayo, J. (2016). How two-dimensional bending can extraordinarily stiffen thin sheets. *Scientific Reports*, *6*(1), 29627. https://doi.org/10.1038/srep29627

Pusok, A., & Kaus, B. J. (2015). Development of topography in 3-D continental-collision models. *Geochemistry, Geophysics, Geosystems*, *16*(5), 1378–1400. https://doi.org/10.1002/2015gc005732

Ramberg, H. (1981). Gravity, deformation and the Earth's crust: In theory, experiments, and geological application. (No Title).

Räss, L., Utkin, I., Duretz, T., Omlin, S., & Podladchikov, Y. Y. (2022). Assessing the robustness and scalability of the accelerated pseudo-transient method. *Geoscientific Model Development*, *15*(14), 5757–5786. https://doi.org/10.5194/gmd-15-5757-2022

Rey, P., Vanderhaeghe, O., & Teyssier, C. (2001). Gravitational collapse of the continental crust: Definition, regimes and modes. *Tectonophysics*, *342*(3), 435–449. (Partial Melting of Crust and Flow of Orogens) https://doi.org/10.1016/S0040-1951(01)00174-3

Ribe, N. M. (2002). A general theory for the dynamics of thin viscous sheets. *Journal of Fluid Mechanics*, *457*, 255–283. https://doi.org/10.1017/s0022112001007649

Ribe, N. M. (2018). *Theoretical mantle dynamics*. Cambridge University Press.

Royden, L. H., Burchfiel, B. C., King, R. W., Wang, E., Chen, Z., Shen, F., & Liu, Y. (1997). Surface deformation and lower crustal flow in eastern Tibet. *Science*, *276*(5313), 788–790. https://doi.org/10.1126/science.276.5313.788

Royden, L. H., Burchfiel, B. C., & van der Hilst, R. D. (2008). The geological evolution of the Tibetan plateau. *Science*, *321*(5892), 1054–1058. https://doi.org/10.1126/science.1155371

Schmalholz, S. M., Duretz, T., Hetényi, G., & Medvedev, S. (2019). Distribution and magnitude of stress due to lateral variation of gravitational potential energy between Indian lowland and Tibetan plateau. *Geophysical Journal International*, *216*(2), 1313–1333. https://doi.org/10.1093/gji/ggy463

Schmalholz, S. M., Kaus, B. J., & Burg, J.-P. (2009). Stress-strength relationship in the lithosphere during continental collision. *Geology*, *37*(9), 775–778. https://doi.org/10.1130/g25678a.1

Schmalholz, S. M., Medvedev, S., Lechmann, S. M., & Podladchikov, Y. (2014). Relationship between tectonic overpressure, deviatoric stress, driving force, isostasy and gravitational potential energy. *Geophysical Journal International*, *197*(2), 680–696. https://doi.org/10.1093/gji/ggu040

Schmalholz, S. M., Podladchikov, Y., & Burg, J.-P. (2002). Control of folding by gravity and matrix thickness: Implications for large-scale folding. *Journal of Geophysical Research*, *107*(B1), ETG–1. https://doi.org/10.1029/2001JB000355

Schmalholz, S. M., & Podladchikov, Y. Y. (2013). Tectonic overpressure in weak crustal-scale shear zones and implications for the exhumation of high-pressure rocks. *Geophysical Research Letters*, *40*(10), 1984–1988. https://doi.org/10.1002/grl.50417

Shi, X., Kirby, E., Furlong, K. P., Meng, K., Robinson, R., & Wang, E. (2015). Crustal strength in central Tibet determined from Holocene shoreline deflection around Siling Co. *Earth and Planetary Science Letters*, *423*, 145–154. https://doi.org/10.1016/j.epsl.2015.05.002

Sun, Y., Li, H., & Fan, T. (2019). A numerical study of lithospheric deformation and strain partitioning across the Longmen Shan orogenic belt, Eastern Tibetan plateau. *Tectonics*, *38*(8), 3108–3123. https://doi.org/10.1029/2019TC005512

Tapponnier, P., Zhiqin, X., Roger, F., Meyer, B., Arnaud, N., Wittlinger, G., & Jingsui, Y. (2001). Oblique stepwise rise and growth of the Tibet Plateau. *Science*, *294*(5547), 1671–1677. https://doi.org/10.1126/science.105978

Thatcher, W., & Pollitz, F. F. (2008). Temporal evolution of continental lithospheric strength in actively deforming regions. *GSA Today*, *18*(4/5), 4. https://doi.org/10.1130/gsat01804-5a.1

Townend, J., & Zoback, M. D. (2000). How faulting keeps the crust strong. *Geology*, *28*(5), 399–402. https://doi.org/10.1130/0091-7613(2000)028<0399:hfktcs>2.3.co;2

Turcotte, D. L., & Oxburgh, E. (1976). Stress accumulation in the lithosphere. *Tectonophysics*, *35*(1–3), 183–199. https://doi.org/10.1016/0040-1951(76)90037-8

Turcotte, D. L., & Schubert, G. (2014). *Geodynamics*. Cambridge University Press.

Virieux, J. (1986). P-SV wave propagation in heterogeneous media: Velocity-stress finite-difference method. *Geophysics*, *51*(4), 889–901. https://doi.org/10.1190/1.1442147

Wang, L. H., Yarushina, V. M., Alkhimenkov, Y., & Podladchikov, Y. (2022). Physics-inspired pseudo-transient method and its application in modelling focused fluid flow with geological complexity. *Geophysical Journal International*, *229*(1), 1–20. https://doi.org/10.1093/gji/ggab426

Warners-Ruckstuhl, K. N., Govers, R., & Wortel, R. (2012). Lithosphere–mantle coupling and the dynamics of the Eurasian plate. *Geophysical Journal International*, *189*(3), 1253–1276. https://doi.org/10.1111/j.1365-246x.2012.05427.x

Warners-Ruckstuhl, K. N., Govers, R., & Wortel, R. (2013). Tethyan collision forces and the stress field of the Eurasian Plate. *Geophysical Journal International*, *195*(1), 1–15. https://doi.org/10.1093/gji/ggt219

Weijermars, R., & Schmeling, H. (1986). Scaling of Newtonian and non-Newtonian fluid dynamics without inertia for quantitative modelling of rock flow due to gravity (including the concept of rheological similarity). *Physics of the Earth and Planetary Interiors*, *43*(4), 316–330. https://doi.org/10.1016/0031-9201(86)90021-x

Yang, J., Kaus, B. J., Li, Y., Leloup, P. H., Popov, A. A., Lu, G., et al. (2020). Lower crustal rheology controls the development of large offset strike-slip faults during the Himalayan-Tibetan orogeny. *Geophysical Research Letters*, *47*(18), e2020GL089435. https://doi.org/10.1029/2020gl089435

Zeitler, P. K., Meltzer, A. S., Koons, P. O., Craw, D., Hallet, B., Chamberlain, C. P., et al. (2001). Erosion, Himalayan geodynamics, and the geomorphology of metamorphism. *GSA Today*, *11*(1), 4–9. https://doi.org/10.1130/1052-5173(2001)011<0004:ehgatg>2.0.co;2

Zhang, P., Chen, L., Xiao, W., & Zhang, J. (2022). Topographic response of Hinterland Basins in Tibet to the India–Asia convergence: 3D thermo-mechanical modeling. *Frontiers in Earth Science*, *10*, 845126. https://doi.org/10.3389/feart.2022.845126

Zhang, P.-Z., Shen, Z., Wang, M., Gan, W., Burgmann, R., Molnar, P., et al. (2004). Continuous deformation of the Tibetan plateau from global positioning system data. *Geology*, *32*(9), 809–812. https://doi.org/10.1130/g20554.1

Zhang, Z., Wang, Y., Chen, Y., Houseman, G. A., Tian, X., Wang, E., & Teng, J. (2009). Crustal structure across Longmenshan fault belt from passive source seismic profiling. *Geophysical Research Letters*, *36*(17), L17310. https://doi.org/10.1029/2009gl039580

Zheng, G., Wang, H., Wright, T. J., Lou, Y., Zhang, R., Zhang, W., et al. (2017). Crustal deformation in the India-Eurasia collision zone from 25 years of GPS measurements. *Journal of Geophysical Research: Solid Earth*, *122*(11), 9290–9312. https://doi.org/10.1002/2017jb014465

Zoback, M. L. (1992). First-and second-order patterns of stress in the lithosphere: The World Stress Map Project. *Journal of Geophysical Research*, *97*(B8), 11703–11728. https://doi.org/10.1029/92jb00132